NASA/TM—2016-219115

Stochastic-Strength-Based Damage Simulation of Ceramic Matrix Composite Laminates

Noel N. Nemeth
Glenn Research Center, Cleveland, Ohio

Subodh K. Mital
University of Toledo, Toledo, Ohio

Pappu L. N. Murthy, Brett A. Bednarcyk, and Evan J. Pineda
Glenn Research Center, Cleveland, Ohio

Ramakrishna T. Bhatt
Ohio Aerospace Institute, Cleveland, Ohio

Steven M. Arnold
Glenn Research Center, Cleveland, Ohio

October 2016

NASA STI Program . . . in Profile

Since its founding, NASA has been dedicated to the advancement of aeronautics and space science. The NASA Scientific and Technical Information (STI) Program plays a key part in helping NASA maintain this important role.

The NASA STI Program operates under the auspices of the Agency Chief Information Officer. It collects, organizes, provides for archiving, and disseminates NASA's STI. The NASA STI Program provides access to the NASA Technical Report Server—Registered (NTRS Reg) and NASA Technical Report Server—Public (NTRS) thus providing one of the largest collections of aeronautical and space science STI in the world. Results are published in both non-NASA channels and by NASA in the NASA STI Report Series, which includes the following report types:

- TECHNICAL PUBLICATION. Reports of completed research or a major significant phase of research that present the results of NASA programs and include extensive data or theoretical analysis. Includes compilations of significant scientific and technical data and information deemed to be of continuing reference value. NASA counter-part of peer-reviewed formal professional papers, but has less stringent limitations on manuscript length and extent of graphic presentations.

- TECHNICAL MEMORANDUM. Scientific and technical findings that are preliminary or of specialized interest, e.g., "quick-release" reports, working papers, and bibliographies that contain minimal annotation. Does not contain extensive analysis.

- CONTRACTOR REPORT. Scientific and technical findings by NASA-sponsored contractors and grantees.

- CONFERENCE PUBLICATION. Collected papers from scientific and technical conferences, symposia, seminars, or other meetings sponsored or co-sponsored by NASA.

- SPECIAL PUBLICATION. Scientific, technical, or historical information from NASA programs, projects, and missions, often concerned with subjects having substantial public interest.

- TECHNICAL TRANSLATION. English-language translations of foreign scientific and technical material pertinent to NASA's mission.

For more information about the NASA STI program, see the following:

- Access the NASA STI program home page at http://www.sti.nasa.gov

- E-mail your question to help@sti.nasa.gov

- Fax your question to the NASA STI Information Desk at 757-864-6500

- Telephone the NASA STI Information Desk at 757-864-9658

- Write to:
  NASA STI Program
  Mail Stop 148
  NASA Langley Research Center
  Hampton, VA 23681-2199

NASA/TM—2016-219115

Stochastic-Strength-Based Damage Simulation of Ceramic Matrix Composite Laminates

Noel N. Nemeth
Glenn Research Center, Cleveland, Ohio

Subodh K. Mital
University of Toledo, Toledo, Ohio

Pappu L. N. Murthy, Brett A. Bednarcyk, and Evan J. Pineda
Glenn Research Center, Cleveland, Ohio

Ramakrishna T. Bhatt
Ohio Aerospace Institute, Cleveland, Ohio

Steven M. Arnold
Glenn Research Center, Cleveland, Ohio

National Aeronautics and
Space Administration

Glenn Research Center
Cleveland, Ohio 44135

October 2016

Acknowledgments

This work was funded by the NASA Transformational Tools and Technologies Project of NASA's Aeronautics Research Mission Directorate.

Level of Review: This material has been technically reviewed by technical management.

Available from

NASA STI Program
Mail Stop 148
NASA Langley Research Center
Hampton, VA 23681-2199

National Technical Information Service
5285 Port Royal Road
Springfield, VA 22161
703-605-6000

This report is available in electronic form at http://www.sti.nasa.gov/ and http://ntrs.nasa.gov/

Stochastic-Strength-Based Damage Simulation of Ceramic Matrix Composite Laminates

Noel N. Nemeth
National Aeronautics and Space Administration
Glenn Research Center
Cleveland, Ohio 44135

Subodh K. Mital
University of Toledo
Toledo, Ohio 43606

Pappu L. N. Murthy, Brett A. Bednarcyk, and Evan J. Pineda
National Aeronautics and Space Administration
Glenn Research Center
Cleveland, Ohio 44135

Ramakrishna T. Bhatt
Ohio Aerospace Institute
Cleveland, Ohio 44142

Steven M. Arnold
National Aeronautics and Space Administration
Glenn Research Center
Cleveland, Ohio 44135

Summary

The Finite Element Analysis—Micromechanics Analysis Code/Ceramics Analysis and Reliability Evaluation of Structures (FEAMAC/CARES) program was used to characterize and predict the progressive damage response of silicon-carbide-fiber-reinforced reaction-bonded silicon nitride matrix (SiC/RBSN) composite laminate tensile specimens. Studied were unidirectional laminates $[0]_8$, $[10]_8$, $[45]_8$, and $[90]_8$; cross-ply laminates $[0_2/90_2]_s$; angled-ply laminates $[+45_2/–45_2]_s$; doubled-edge-notched $[0]_8$ laminates; and central-hole laminates. Results correlated well with the experimental data. This work was performed as a validation and benchmarking exercise of the FEAMAC/CARES program.

FEAMAC/CARES simulates stochastic-based discrete-event progressive damage of ceramic matrix composite and polymer matrix composite material structures. It couples three software programs: (1) the Micromechanics Analysis Code with Generalized Method of Cells (MAC/GMC), (2) the Ceramics Analysis and Reliability Evaluation of Structures Life Prediction Program (CARES/*Life*), and (3) the Abaqus finite element analysis program. MAC/GMC contributes multiscale modeling capabilities and micromechanics relations to determine stresses and deformations at the microscale of the composite material repeating-unit-cell (RUC). CARES/*Life* contributes statistical multiaxial failure criteria that can be applied to the individual brittle-material constituents of the RUC, and Abaqus is used to model the overall composite structure. For each FEAMAC/CARES simulation trial, the stochastic nature of brittle material strength results in random, discrete damage events that incrementally progress until ultimate structural failure.

1.0 Introduction

This report examines the capability of the Finite Element Analysis Micromechanics Analysis Code/Ceramics Analysis and Reliability Evaluation of Structures (FEAMAC/CARES) (Nemeth et al., 2016) stochastic-strength-based damage simulation software tool to predict the damage response of various ceramic matrix composite (CMC) laminate configurations loaded in tension. Unidirectional laminates $[0]_8$, $[10]_8$, $[45]_8$, and $[90]_8$; cross-plied laminates $[0_2/90_2]_s$; angled-ply laminates $[+45_2/-45_2]_s$; doubled-edge notched $[0]_8$; and central-hole laminates composed of silicon carbide fibers embedded in a reaction-bonded silicon nitride matrix (SiC/RBSN) were studied. The experimental data were generated from rupture tests performed by Bhatt and Phillips (1990) on rectangular tensile specimens (except for the tests with central-hole laminates, which were studied to contrast the predicted failure modes against notched specimen geometry). This particular experimental data set covers a range of conditions and has been well documented experimentally and analytically. We chose it because of the amount and variety of configurations that were tested—making it a good model material for our validation/benchmarking exercise. In addition, laminated CMCs are less complex than woven composites: their failure modes are more isolated from the additional geometrical/curvature effects induced from the weaving (i.e., fibers are aligned straight instead of having undulations or curvature as produced in weft or warp weaves). This simplified the failure physics that we wanted to capture and model.

The damage simulations were performed using the FEAMAC/CARES software. The process involved calibrating the stress-strain behavior for the laminate with 0°-oriented fibers and then predicting the response for the other laminate configurations.

Symbols

$\overline{C}$	Shetty shear-sensitivity coefficient (see Nemeth et al., 2005, 2016).
E	Young's modulus
m_V	Weibull modulus for volume-based analysis
n	integer; number of composite layers
x_1, x_2, x_3	global coordinate system
x_1', x_2', x_3'	local material coordinate system
α_L, α_T	longitudinal and transverse coefficients of thermal expansion
ν	Poisson's ratio
σ_{oV}	Weibull scale parameter normalized to volume
$\sigma_{11}, \sigma_{22}, \sigma_{33}$	stress components parallel to the x_1, x_2, and x_3 directions

2.0 Silicon-Carbide-Fiber-Reinforced/Reaction-Bonded Silicon Nitride Background

Details regarding the fabrication and properties of the SiC/RBSN system can be found in Bhatt (1988), Bhatt and Phillips (1990), Chulya et al. (1991), and Saigal et al. (1993). The starting materials for the composites were SiC fiber mats and silicon powder cloth. The SiC fiber was double-coated SCS–6 manufactured by Textron Specialty Materials Division. The fibers had an average outer diameter of 142 μm and included a thin carbon-rich coating over a SiC substrate. The SiC fiber sheath was produced by chemical vapor deposition over the smaller pyrolitic graphite-coated carbon core. Composite fabrication involved four steps: fabrication of SiC fiber mats, fabrication of silicon tapes, consolidation of preform by warm-pressing alternate layers of fiber mats and silicon tapes in a vacuum hot press, and

nitridation of SiC/Si preforms at appropriate conditions (approximately 1250 °C) to convert silicon to silicon nitride (Si_3N_4) matrix. The various laminates that were produced each consisted of 8 fiber plies in a fully densified matrix with an approximately 30-vol% fibers (except where noted in Chulya et al., 1991, for 24-vol% fibers).

The outer carbon layer on the fiber resulted in a very weak fiber/matrix interface, with a thickness equal to about 3 percent of the fiber diameter. The carbon-rich coating acted as a very weak interfacial material between the fiber and the Si_3N_4 matrix material. As described by Bhatt and Phillips (1990), tensile stress-strain response was determined for laminates with $[0]_8$, $[10]_8$, $[45]_8$, $[90]_8$, $[0_2/90_2]_s$, and $[+45_2/–45_2]_s$ ply layups. This is shown in Figure 1 (adapted from Bhatt and Phillips, 1990). The figure does not show the actual stress-strain behavior of the individual specimens but represents the averaged behavior of individual specimens (typically three or four specimens). For example, for the $[0]_8$ laminate, the stress-strain behavior is shown schematically as being composed of two straight lines (bilinear behavior). This simplification omits the important detail near the knee portion (Bhatt, private communication, 2014). However, the onset of matrix cracking or "first matrix cracking" is indicated at the figure at ~230 MPa followed by serrations where the stress on the specimen momentarily dropped and then recovered. The $[0]_8$ and $[0_2/90_2]_s$ stress-strain curves displayed bilinear behavior, having an initial linear-elastic response for the undamaged material at low load levels. At higher load levels, matrix cracking began and eventually saturated the CMC with a regular pattern of crack spacing. Afterward, only the intact fibers held the CMC together as the load increased until the final composite failure. The $[90]_8$, $[10]_8$, and $[45]_8$ laminate stress-strain curves had a linear-elastic response until a sudden brittle failure.

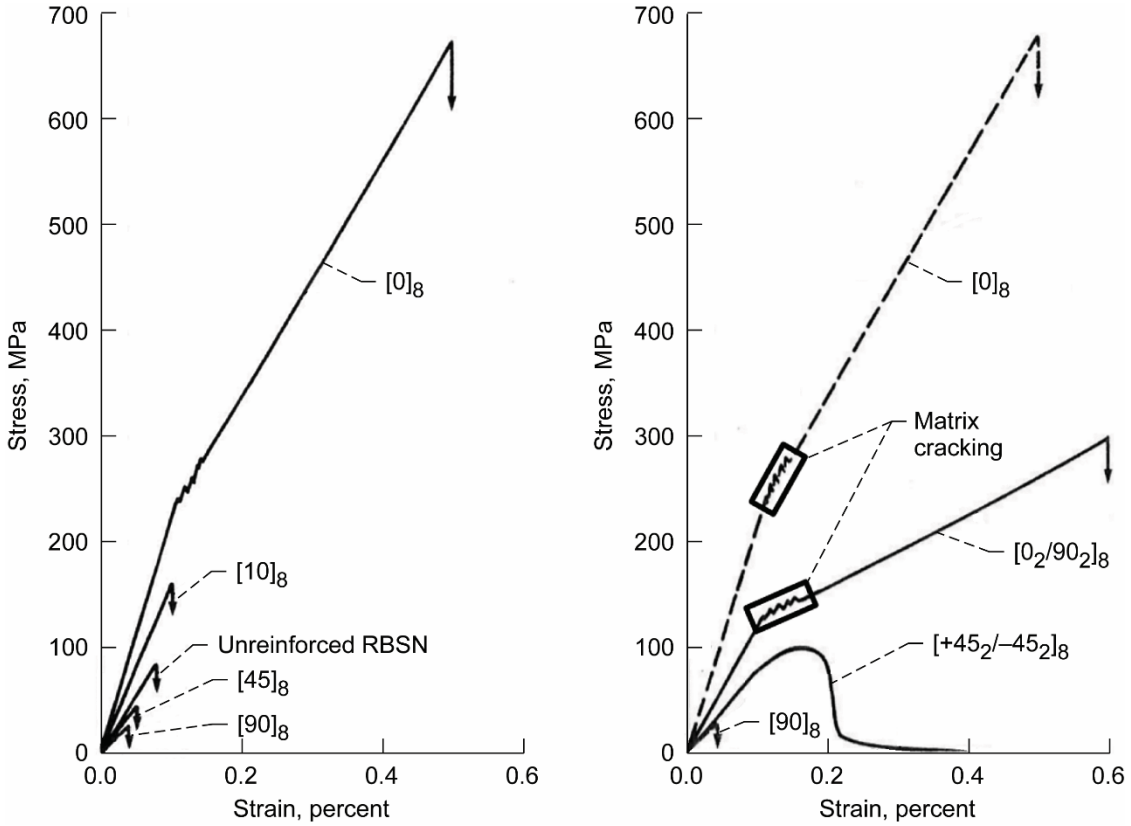

Figure 1.—Tensile stress-strain response for $[0]_8$, $[10]_8$, $[45]_8$, $[90]_8$, $[0_2/90_2]_s$, and $[+45_2/–45_2]_s$ ply layups. RBSN, reaction-bonded silicon nitride. From Bhatt and Phillips, 1990. Copyright © 1990 ASTM International; used with permission.

The failure initiated with simple matrix cracking. This was followed by fiber/matrix debonding and then ultimate specimen failure due to fibers breaking in a brittle manner (Bhatt and Phillips, 1990). The $[+45_2/-45_2]_s$ stress-strain curve displayed an initial elastic response followed by matrix damage and a more gradual softening of the stress-strain curve. Notched specimens were also tested by Bhatt and Phillips (1990), and these results are also described and simulated herein. There was a significant statistical variation in the composite material response (Bhatt and Phillips, 1990), and both the constituent properties and effective response of ceramic matrix composites are known in general to be highly stochastic (Lamon, 2001; Liu and Arnold, 2011; Murthy et al., 2008).

In the experiments conducted by Bhatt and Phillips (1990), specimens with dimensions of 125 by 12.7 by 1.2 mm were prepared for tensile testing. Glass-fiber-reinforced epoxy tabs were adhesively bonded at the specimen ends leaving 25 mm of exposed material as the test gauge length for most of the specimens. For some specimens the gauge length was varied from 12 to 50 mm in order to study the effect of gauge length on the strength response. For this report we only looked at the specimen with the 25-mm gauge length and did not study the issue of size effect with the other specimen gauge lengths.

3.0 Analysis Setup

3.1 Material Properties

The fiber Young's modulus used was 390 GPa as measured by DiCarlo and Williams (1980), and the matrix Young's modulus of 110 GPa was measured from Bhatt and Phillips (1990). This CMC material was subsequently analyzed by Murthy et al. (1996) and Goldberg (2012) and included these property values. In this report we used the same constituent properties as in Murthy et al. (1996) and Goldberg (2012), with the exception that the thermal expansion coefficients of the fiber in the axial and transverse direction were assumed to be different (anisotropic). We did this because for this material Saigal et al. (1993) states that "the fiber is orthotropic, with different coefficients of thermal expansion along and perpendicular to the fiber-axis." Saigal et al. (1993) estimated the thermal residual strains and stresses from measurements taken using neutron diffraction of specimens and augmented with results from finite element analysis. Murthy et al. (1996) and Goldberg (2012) used the same thermal expansion coefficient of 4.1×10^{-6} in the axial and transverse direction for the fiber. Murthy et al. (1996), Goldberg (2012), and Saigal et al. (1993) all assumed that the individual material constituents of the CMC composite have isotropic property behavior for the Young's modulus and Poisson's ratio. The material properties that we used for the analysis are listed in Table I. We assumed that the material properties did not change with temperature. The particular value used for the transverse coefficient of thermal expansion for the fiber is explained later.

TABLE I.—CONSTITUENT PROPERTIES OF SiC/REACTION-BONDED SILICON NITRIDE (RBSN) WITH ANISOTROPIC THERMAL EXPANSION COEFFICIENTS

Constituent	Modulus, E, GPa	Poisson's ratio, ν	Longitudinal coefficient of thermal expansion, α_L, m/m/°C	Transverse coefficient of thermal expansion, α_T, m/m/°C
Fiber	390	0.17	4.1×10^{-6}	1.84×10^{-6}
Matrix	110	.22	2.2	2.2
Interface	1.8	.22	2.0	2.0

3.2 Estimating Internal Residual Stresses and Effect of Anisotropic Thermal Expansion Coefficient

As the material cools down from its processing temperature (the temperature from which it was made), residual stresses build up in individual composite material constituents. These residual stresses result from the difference in the thermal expansion rates between the individual material constituents of the joined (bonded) materials as the composite cools down. When the composite is made at an elevated temperature, the different material constituents bond together and all material constituents are in equilibrium—they have no internal stresses (are stress free). As the composite cools, these residual stresses build up within the individual material constituents although the composite itself maintains an overall equilibrium. The "stress-free" temperature and the temperature at which the composite was made can be different because material creep mechanisms may be active. As such, the actual residual stresses in the composite may not be well correlated with the original processing temperature. In this report we do not consider creep deformation processes. Instead, to impart residual stresses in the material constituents, we correlate a stress-free starting temperature with the measured room-temperature material stress-strain response for a 0°-oriented unidirectional ply loaded in uniaxial tension and applied parallel to the fiber direction back.

We used the MAC/GMC code (a stand-alone version not coupled with finite element analysis), which employs the generalized method of cells (GMC) micromechanics theory (Aboudi et al., 2013), to estimate the residual stress field in the fiber, interface, and matrix as a function of cooldown temperature from an initial stress-free condition. We used a repeating unit-cell (RUC) composite fiber architecture available in the MAC/GMC code to analyze a continuous-fiber-reinforced CMC. Figure 2 shows the standard unit-cell architecture used, which is an option available in MAC/GMC. The use of only 16 subcells (in a 4×4 configuration) substantially reduces the computational overhead in the multiscale FEAMAC/CARES analysis, but this is at the expense of the level of fidelity (detail and accuracy) that can be obtained in the stress fields within the unit cell architecture. These are some of the tradeoffs that are involved in the analysis.

In our analysis we found that residual tensile stresses in some of the subcells in the RUC composed of matrix material built up rapidly as the composite cooled down from an initial stress-free temperature when the fiber thermal expansion coefficient was assumed to be isotropic (having the same value along the fiber axis and transverse to the fiber axis). This posed a potential problem because high tensile stresses in the matrix could lead to premature failure or could prevent one from using a higher stress-free temperature in the analysis. This rate of stress build up is reduced when anisotropic fiber thermal expansion coefficients are used. The fact that Saigal et al. (1993) stated, "the fiber is orthotropic, with different coefficients of thermal expansion along and perpendicular to the fiber-axis," provides a physical justification for using anisotropic thermal expansion coefficients for the fiber in our analysis. To investigate this we examined three different combinations of longitudinal and transverse fiber thermal expansion coefficients. One combination was isotropic, where both were equal, and two cases were not equal.

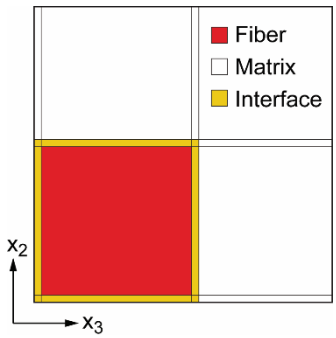

Figure 2.—Fiber-reinforced composite 4×4 subcell repeating-unit-cell (RUC) architecture used in the FEAMAC/CARES analysis.

Figure 3 shows the predicted, average residual stresses from MAC/GMC at room temperature (23 °C) that develop in a specific matrix subcell versus an initial stress-free applied temperature load for the isotropic case and two combinations of anisotropic thermal expansion coefficient of the fiber. The same thermal expansion coefficient of 4.1×10^{-6} as used by Murthy et al. (1996) and Goldberg (2012) was used for the fiber direction, but the value was reduced transverse to the fiber direction for the two cases investigated. The two anisotropic thermal expansion coefficient combinations provided a best case and an intermediate case scenario that reduced the rate of the buildup of tensile residual stresses with cooldown temperature. The matrix subcell located directly above the fiber subcell (Fig. 2) was examined. This particular subcell provided equal-to or worst-case tensile stresses in comparison to other matrix subcells and would be an initiation point of matrix failure in the RUC during cooldown. Note that the stresses in the matrix subcell located to the right of the fiber subcell in Figure 2 have the same magnitude as those in the subcell located directly above the fiber subcell, except that they are rotated 90° because of the symmetry of the RUC. The thermal expansion coefficients for the matrix and interface were kept constant, as listed in Table I. The stresses were obtained from MAC/GMC output. The stress component directions correspond to the spatial coordinate system shown in Figure 2. The fiber direction is parallel to the x_1 axis. Three combinations of fiber thermal expansion coefficients were tried. One case used values of $\alpha_L = 4.1\times10^{-6}$ m/m/°C and $\alpha_T = 4.1\times10^{-6}$ m/m/°C applied longitudinally and transversely, respectively, to the fiber-axis direction (case 1 in Fig. 3). This corresponded to the fiber thermal expansion coefficient being isotropic. The second case used values of $\alpha_L = 4.1\times10^{-6}$ m/m/°C and $\alpha_T = 2.0\times10^{-6}$ m/m/°C applied longitudinally and transversely, respectively, to the fiber-axis direction (case 2 in Fig. 3). The third case used values of $\alpha_L = 4.1\times10^{-6}$ m/m/°C and $\alpha_T = 1.84\times10^{-6}$ m/m/°C applied longitudinally and transversely, respectively, to the fiber-axis direction (case 3 in Fig. 3). The second and third cases were for anisotropic fiber thermal expansion coefficients.

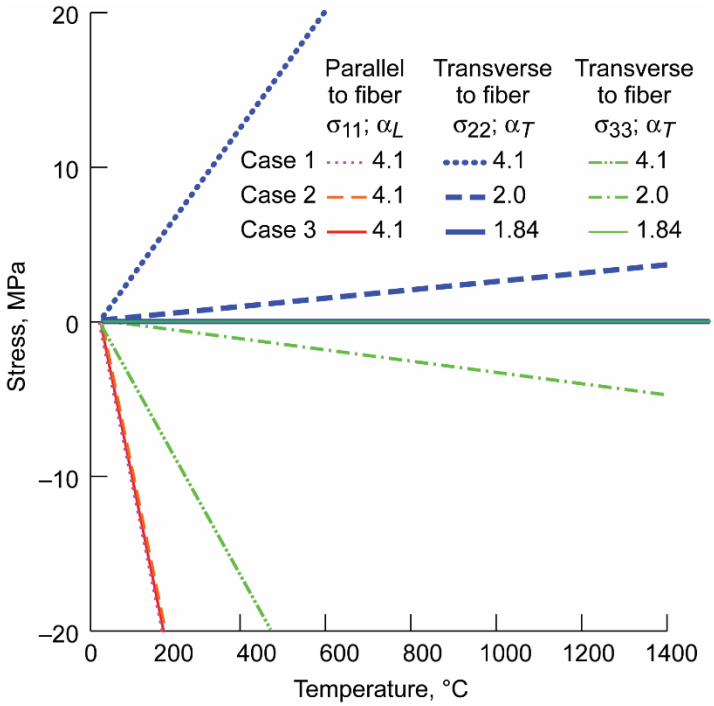

Figure 3.—Effect of isotropic and anisotropic thermal expansion coefficients of the fiber on the residual stresses that develop in the matrix subcell located directly above the fiber subcell shown in Figure 2. Here, α_L and α_T are longitudinal and transverse coefficients of thermal expansion, and σ_{11}, σ_{22}, and σ_{33} are stress components parallel to the x_1, x_2, and x_3 directions.

Figure 3 shows that the predicted response is strongly influenced by the values chosen for the expansion coefficients for this particular subcell. The stress components σ_{22} and σ_{33} do not have the same value because the square-packed arrangement of the fiber in the RUC causes stress concentrations to develop nonuniformly (but symmetrically) around the fiber. For the isotropic case (case 1), where $\alpha_L = \alpha_T = 4.1\times10^{-6}$ m/m/°C, there is a rapid buildup of the σ_{22} stress component in tension as the applied stress-free temperature increases. This becomes a problem because the matrix will not tolerate tensile stresses beyond a certain level and will fail prematurely during the cooldown phase, limiting the practical range of temperature that can be considered. However, for the two cases where the fiber thermal expansion coefficient is anisotropic, the tensile residual stresses in the matrix are greatly reduced versus the applied stress-free temperature. For case 3, where $\alpha_L = 4.1\times10^{-6}$ m/m/°C and $\alpha_T = 1.84\times10^{-6}$ m/m/°C, the tensile residual stresses essentially vanish or are insignificant. In this case premature tensile failure cannot occur in the matrix regardless of the value of the applied stress-free temperature. This is an important consideration when our model is calibrated to experimental data. In our analysis we assume the most favorable condition, $\alpha_L = 4.1\times10^{-6}$ m/m/°C and $\alpha_T = 1.84\times10^{-6}$ m/m/°C, where tensile residual stresses from the cooldown in the matrix of the RUC are minimized. Saigal et al. (1993) used $\alpha_L = 4.7\times10^{-6}$ m/m/°C and $\alpha_T = 2.63\times10^{-6}$ m/m/°C for a ratio of 0.56. In our case we assumed that $\alpha_L = 4.1\times10^{-6}$ m/m/°C and $\alpha_T = 1.84\times10^{-6}$ m/m/°C for a ratio of 0.45. This ratio is reasonably close to the measured values and acceptable for the purpose of this demonstration/benchmark problem.

3.2.1 Finite Element Model Setup

For the FEAMAC/CARES analysis, the gauge section of a 25- by 12.7- by 1.2-mm rectangular tensile specimen was modeled using Abaqus (Dassault Systèmes Simulia Corp., 2011) S4-type shell elements. The finite element mesh was composed of 10×20 equally sized elements. The S4 element type is suitable for large strain analysis. It has 12 gaussian integration points per composite ply layer—arranged in a three-layer stack through the thickness with four gaussian integration points in each stack. This shell element can be composed of *n* multiple composite layers where the total number of integration points in the element is $n \times 12$.

Each ply layer can be associated with an RUC architecture as described in Bednarcyk and Arnold (2006, 2002a,b). For our analysis, we used the RUC architecture shown in Figure 2. This is also reproduced in Figure 4, which shows the finite element mesh for the specimen gauge section and the RUC architecture that is applied at each shell element gaussian integration point. The fiber direction in each ply is specified in the Abaqus input file. Figure 4 depicts the 0° fiber direction of the unidirectional ply. For the finite element model, appropriate boundary conditions were imposed and a monotonically increasing displacement over time was applied at the top of the specimen in the direction parallel with the length in order to simulate the specimen stress-strain response. To reduce the computational effort for unidirectional laminates, instead of simulating multiple layers, we simulated a single-ply layer. Boundary conditions specific for the various on-axis and off-axis loadings are discussed in subsequent sections of this report.

The Abaqus input deck (input file: *.inp) that we constructed for this problem consisted of four separate, but sequential, loading conditions (steps), where the results from the previous loading condition were used as the initial condition for the subsequent loading condition. The steps were designed so that different regions of the stress-strain response curve could be examined to an arbitrary level of detail (broken up into more solution increments or less solution increments over the region of the stress-strain curve to be examined) as warranted. The first condition (load step 1) was the thermal cooldown, which was done to impart residual stresses on the individual material constituents. The simulation of the specimen began with an initial stress-free elevated temperature. Over the course of several time increments (arbitrarily over 10 equally spaced increments—we found that using too few increments could cause the program to abort), the specimen was cooled to room temperature (23 °C). The cooling was imparted as a "ramp" load. For the off-axis-loaded unidirectional plies, the cooling distorted the original rectangular specimen to a parallelogram. (However, the specimen did not warp and remained flat.)

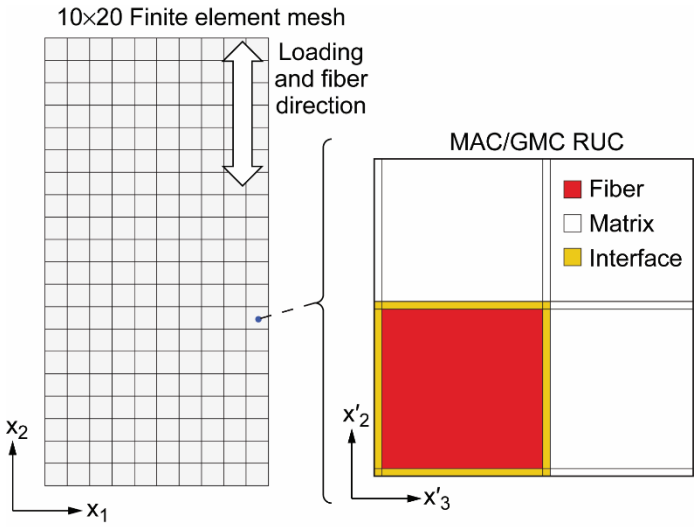

Figure 4.—Finite element model of tensile specimen gauge area and MAC/GMC 4×4 subcell repeating unit cell (RUC) architecture used in the problem simulation at the element gaussian integration point. Here x_1, and x_2 denote the global coordinate system reference frame and x_2' and x_3' denote the local material coordinate system reference frame.

A single node along the bottom specimen edge approximately at the midpoint along the edge was fixed for the three displacement directions (1, 2, and 3) and one rotational degree of freedom (5). A single node approximately at the midpoint of the top edge of the specimen was fixed for the displacement directions (1 and 3) and one rotational degree of freedom (5). These boundary conditions allowed the specimen to freely contract as the temperature was lowered while preventing rigid-body modes.

The results from the thermal cooldown load step were used as the initial starting condition for the next loading sequence (load step 2). This loading sequence imparted a ramp displacement (in direction 2) along the top edge of the specimen, consistent with the uniaxial loading of a tensile specimen. This was applied over 10 equally spaced displacement increments. The bottom edge was constrained (in direction 2). The objective of this load condition sequence was to simulate the linear elastic regime of the stress-strain curve using only a relatively few number of ramping load increments. We could do this because in this region of the response the likelihood of any damage was very low. Furthermore, by using only a relatively few number of ramping load increments in this regime of the stress-strain response, we could reduce the total execution time as well as memory resources for the simulation. The spanning strain range for this load step, which was set arbitrarily on the basis of previous experience, is listed in subsequent tables (Tables III to X) for the various loading and laminate configurations that were simulated.

The end results from the first ramp loading sequence were used as the initial starting condition for the next loading sequence (load step 3). This loading sequence also imparted a ramp displacement (in direction 2) along the top edge of the specimen consistent with uniaxial loading of a tensile specimen. This was applied over many (usually 100 or more) equally spaced displacement increments. The objective of this load step was to obtain a detailed look at the evolution of the damage in the matrix of the CMC, in the transition region of the stress-strain curve (the nonlinear part), from the beginning of matrix damage initiation up to some point after matrix damage saturation. Also, because many increments were used over this transition region, the simulation more closely approached a converged solution where damage had reached an equilibrium before proceeding to the next displacement increment.

The end results from the second ramp loading sequence (load step 3) were used as the initial starting condition for the next loading sequence (load step 4). This loading sequence also imparted a ramp displacement (in direction 2) along the top edge of the specimen consistent with uniaxial loading of a

tensile specimen. This was applied over many (usually 100 or more) equally spaced displacement increments. The objective of this load step was to span the remaining portion of the stress-strain curve past the point of full fiber failure and hence the complete breakage of the specimen.

3.2.2 Model Calibration

The modeling methodology and description of parameters for the stochastic-strength-based failure criteria are described in Nemeth et al. (2016), and the composite micromechanics and multiscale modeling approach are described in Aboudi et al. (2013) and Bednarcyk and Arnold (2002a). The FEAMAC/CARES simulations were calibrated to experimental data from Chulya et al. (1991) for the stress-strain response of a SiC/RBSN CMC specimen with 24-vol% 0°-oriented fibers under uniaxial tension. Figure 5 shows this stress-strain response curve, which is a complete response curve for an individual specimen as opposed to the bilinear approximation shown in Bhatt and Phillips (1990) and reproduced in Figure 1. Table II lists a set of Weibull parameters that were found to satisfactorily fit this data. For the simulation, the total imposed displacement on the specimen was 0.2 mm for 0.008 strain over the 25-mm gauge length. Table III provides the breakdown of the three sequential load steps of displacement, showing the strain range of each load step, the number of displacement increments, and the displacement imposed per each increment. The Weibull parameters in Table II were obtained through trial and error. Because each parameter affects a specific behavior on the stress-strain curve, a set of parameters that closely fit to the experimental data can be found by successively updating parameter values after each simulation. A Weibull modulus of m_V =20.0 was chosen arbitrarily for the fiber. That value was sufficiently high that strength scatter in the fiber (bundle) would be relatively small. The combination of the higher Weibull modulus and a scale parameter of σ_{oV} = 2875 MPa • mm^{3/m_V} meant that the likelihood of a fiber failing

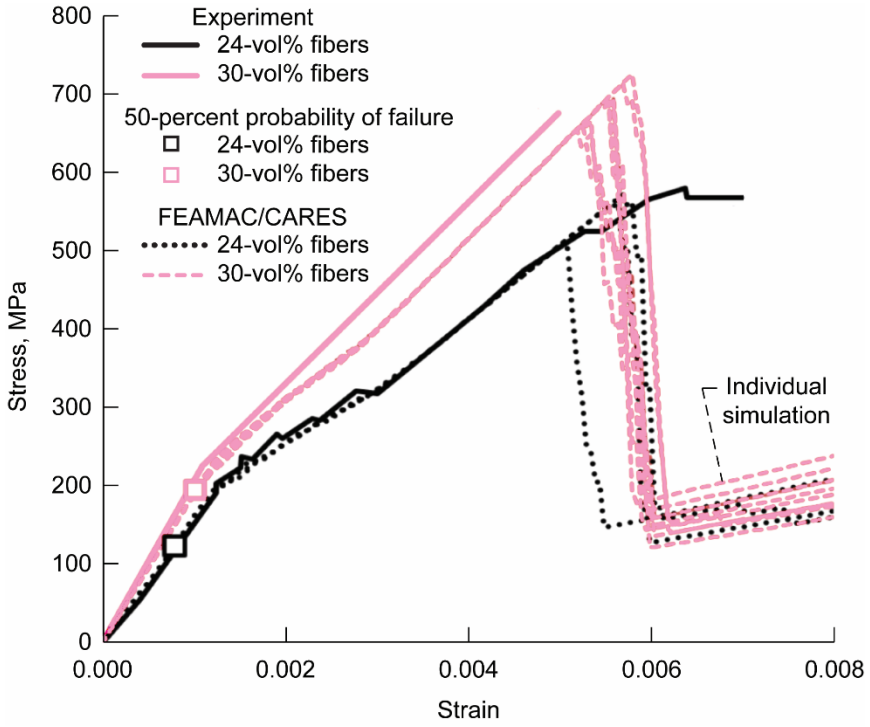

Figure 5.—Experimental stress-strain results for a SiC/reaction-bonded silicon nitride (RBSN) ceramic matrix composite (CMC) specimen with 0°-oriented fibers under uniaxial tension and individual FEAMAC/CARES simulations.

TABLE II.—WEIBULL PARAMETERS USED IN THE SIMULATIONS

Constituent	Weibull modulus, m_V	Weibull scale parameter, σ_{oV}, MPa • mm$^{3/m_V}$
Fiber	20.0	2875.0
Matrix	5.0	150.0
Interface	5.0	80.0[a]

[a]Large value assigned so that early failure in the interface material was suppressed.

TABLE III.—LOAD STEP DESCRIPTION FOR SIMULATION OF SPECIMENS WITH 0°-ORIENTED 24- AND 30-vol% FIBERS

[Total imposed displacement, 0.2 mm for 0.008 strain.]

Stress-strain curve region	Total displacement and strain	Strain range	Number of displacement increments	Displacement per increment, mm
First stage (load step 2)— Elastic response and no damage	0.0175 mm for 0.0007 strain	0.0 to 0.0007	10	0.00175
Second stage (load step 3)— Matrix cracking	0.075 mm for 0.003 strain	0.0007 to 0.003	200	.0002875
Third stage (load step 4)— Fiber controlled until ultimate failure	0.2 mm for 0.008 strain	0.003 to 0.008	100	.00005

before matrix microcracking reached saturation in the specimen was low—an attribute that we desired for this benchmark/demonstration problem. The Weibull scale parameter σ_{0V} for the interface also was set to an arbitrarily large value so that the initial failure usually occurred in the matrix. We did this because the physics for interfacial failure modes and sliding resistance are not accounted for in this version of FEAMAC/CARES or in the MAC/GMC RUC architecture chosen. A stress-free temperature of 550 °C also was used in the simulations.

A fast-fracture rupture analysis was performed using the Weibull parameters shown in Table II for the fiber, matrix, and interface. Isotropic strength response material constituents were assumed, and the analysis was performed with the unit sphere multiaxial model assuming a penny-shaped crack geometry and a Shetty shear-sensitivity constant of $\overline{C}$ = 1.0 (see Nemeth et al., 2005). Shell element volume was indirectly accounted for with a multiplication factor of the shell element thickness times the surface area of the element. This version of FEAMAC/CARES does not account for the effects of stress gradients through the thickness of the shell element in the calculations of element failure probability; therefore, situations involving flexural loading cannot be analyzed. The shell element requires a proper through-the-thickness Weibull stress-volume integration calculation that was not implemented in this version of FEAMAC/CARES. This issue is less of a problem when solid elements are used in the finite element modeling because the effects of through-the-thickness element stress gradients can be reasonably captured at the element integration points that span the element. For the shell element type used here, the through-the-element-thickness stress gradient is provided only as an additional Abaqus output item. Accounting for that additional item was not considered here. For solid elements though, an adequately dense mesh density is required (in regions where stress gradients exist) in order to obtain satisfactory solution accuracy or solution convergence. The cellular automaton feature was turned on for these FEAMAC/CARES simulations (see Nemeth et al., 2016).

In Figure 5, the stress-strain curves for the three simulations (for the SiC/RBSN CMC specimen with 0°-oriented fibers under uniaxial tension), the specimen with 24-vol% fibers matched the experimental data from Chulya et al. (1991) well. The three simulations showed similar behavior with little variation from one to another except at the highest stresses where fiber failure was occurring. Running more simulations of this specimen was not necessary. The “graceful failure” behavior in the nonlinear portion

of the stress-strain curve (approximately between 0.0015 and 0.0035 strain) where matrix cracking occurred was appropriately reproduced in the simulations. In all the simulations a stress-free temperature of 550 °C was used. This value was determined by fitting the simulations to the experimental data for the 24-vol%-fiber specimen in the strain region after matrix crack saturation where only the fiber controlled the stress-strain response. In Figure 5 this region is approximately between 0.003 and 0.005 strain. As the stress-free temperature increases, this portion of the stress-strain curve shifts (translates) to the left. Extrapolating this curve to the zero stress axis means that the curve intercepts the strain axis at some value of compressive (negative) stress. As the stress-free temperature increases, the curve intercepts the strain axis at larger values of compressive stress. What this means is simply that prior to tensile loading a residual tensile stress existed in the fibers. After matrix cracking, this residual stress in the fibers was relieved. When the MAC/GMC program itself was run (outside of FEAMAC), the residual axial stress in the fiber corresponded to 163 MPa. This is lower than the values reported in Saigal et al., (1993), but it is representative. Saigal et al. (1993) uses different elastic and thermal expansion constants than we use in this report, so a direct comparison cannot be made. Their finite element model of a fiber embedded in a matrix unit cell also did not include an interfacial layer. However it is important to note here that a higher stress-free temperature shifts the fiber-controlled curve too far to the left, which does not fit well to the experimental data curve for the specimen with 24-vol% fibers. This is the basis for finding a stress-free temperature appropriate for this CMC material system.

In the fiber-controlled portion of the stress-strain response (approximately between 0.003 and 0.005 strain) for the specimen with 24-vol% fibers, the effect of matrix fragments (uncracked portions of matrix still attached to fibers) on the stress-strain response is not considered. We assume that this region of the stress-strain curve is controlled only by the response of bare fibers. Also shown in Figure 5 for the specimen with 24-vol% fibers is a small box at about 0.0008 strain, indicating a CARES/*Life*-calculated 50-percent probability of matrix failure of the whole tensile specimen prior to the first damage initiation event. Note that, at this level of strain, 50 percent of the simulations would have had a first damage event prior to this point. So this data point was obtained from a simulation that did not have a first damage initiation event by 0.0008 strain. FEAMAC/CARES calculates probabilities of the failure of the whole specimen for the individual material constituents up to the point of the first damage initiation event. Once the first damage initiation event has occurred in a simulation, the CARES/*Life*-calculated probabilities of failure become meaningless. CARES/*Life* tracks specimen probability of failure at each loading increment in a simulation. This is very valuable information to the design engineer who wants to determine a level of loading associated with a probability of having a first damage initiation event. Initiation of damage results in environmental penetration into the CMC and will lead to further damage propagation and material degradation surrounding the damaged region.

Figure 5 shows the stress-strain curves for 10 simulations of the SiC/RBSN CMC specimen with 0°-oriented 30-vol% fibers under uniaxial tension. Table III provides the breakdown of the three sequential load steps of displacement, showing the strain range of each load step, the number of displacement increments, and the displacement imposed per each increment for this specimen volume fraction. The simulation results shown in Figure 5 do not compare as well with the experimental results curve for 0°-oriented 30-vol% fibers. However, that experimental results curve was a bilinear line reproduced from Bhatt and Phillips (1990), and the actual stress-strain curves of the individual specimens was not recorded. The experimental results shown are only an approximation of the observed behavior. In that light, the fit to the experimental data is quite acceptable, particularly at the “knee” in the curve where matrix microcracking was occurring (between 0.001 and 0.002 strain), often denoted as the proportional limit strain (PLS). There is very little visible variation (visible deviation) from one simulation to another in the strain range from 0 to about 0.005 strain. This trend is consistent with the three simulations for the specimen with 24-vol% fibers. The “graceful failure” behavior in the nonlinear portion of the stress-strain curve (approximately between 0.0010 and 0.0030 strain) where matrix cracking occurred was appropriately reproduced in the simulations.

At this point one would be tempted to conclude that the lack of visible variation from one simulation to another in the matrix cracking region of the stress-strain curve, as shown in Figure 5, would allow for a more simplistic deterministic damage model to be substituted for the stochastic analysis as described here and in Nemeth et al. (2016). That would be a short-sighted and misleading conclusion. First, the stochastic-strength-based analysis was required to determine a level of probability for the first damage initiation event as displacement loading progressed. Repeated simulations would show that there is a great deal of scatter of the load level (applied stress) where this first damage event would occur. Second, as will be shown subsequently in this report, this methodology predicts substantial scatter in proportional limit strength. Third, scatter in the composite strength response can be very pronounced depending on loading conditions, such as off-axis loading, which is demonstrated in Section 3.3, for example. Finally, scatter in damage response becomes very evident when time-dependent or cycle-dependent load scenarios are considered as demonstrated in Nemeth et al. (2016). Accounting for the stochastic strength behavior of the CMC material constituents is essential in any prediction regarding the safe design loads, safety margins, and useful service life of CMC components. None of these important effects can be obtained from a deterministic analysis alone.

Figure 6 shows the damage progression for two simulation trials (Figs. 6(a) and (b)) for the 0° tensile specimen with 30-vol% fibers. The cellular automaton feature (as described in Nemeth et al., 2016) was turned on (was fully active). Damage progression is shown from left to right for early matrix damage, followed by the development of substantial matrix damage, followed by early fiber damage, followed by final composite failure. Figure 6 shows the development of organized damage patterns consisting of rows of failed matrix material as matrix failure developed. This is followed by the initial development of fiber failure (which occurred after the matrix had fully failed) and subsequently the final failure of the composite, where a connected path of elements with fiber failure spanning from one side of the specimen to the other side of the specimen can be seen. Table IV provides the applied strain levels and reaction stresses for Figure 6.

The loading profile of the Abaqus input file was constructed so that various portions of the stress-strain curve could be analyzed with any desired number of imposed displacement increments spanning a load step. The initial linear-elastic region of low applied displacement (low strain) where there was no damage in the specimen could be traversed with only a few displacement increments, whereas the portion of the stress-strain curve where matrix damage was developing could be examined in more detail using many small displacement loading increments. This was a computationally efficient approach to solving the problem. Figure 7 shows another set of results for 10 simulations (a different set from Fig. 5) for the tensile specimen with 30-vol% 0°-oriented fibers. The load step investigated a narrow portion of the stress-strain curve between 0.0007 and 0.003 strain. This was broken up into 200 loading increments of 0.0000115 strain. The figure shows a portion of this strain range between 0.0011 and 0.0015 strain. The variation in the stress-strain behavior from one simulation to another is now evident. This variation was not seen as easily in Figure 5 in the region of the curve where matrix cracking was occurring (between 0.001 and 0.003 strain). This is partly due to the scale of the plot shown and partly due to fewer load increments being used in Figure 5 to span the matrix microcracking region, so damage had less of an opportunity to fully develop over the range of strain (the number of loading increments per range of strain). Figure 7 also shows three lines. The first line is extrapolation of the linear-elastic behavior of the CMC prior to any damage initiation event. The second line, shows this same linear-elastic behavior line offset by 0.00005 strain (0.005-percent-strain offset), and the third line shows this same linear-elastic behavior line offset by 0.00010 strain (0.01-percent-strain offset). The second line (0.005-percent-strain offset) is the so-called PLS-offset line (see Kalluri et al., 2004), which is a measure by which there is noticeable deviation from linear-elastic behavior. The positions where each simulation trial intersects this line also are indicated.

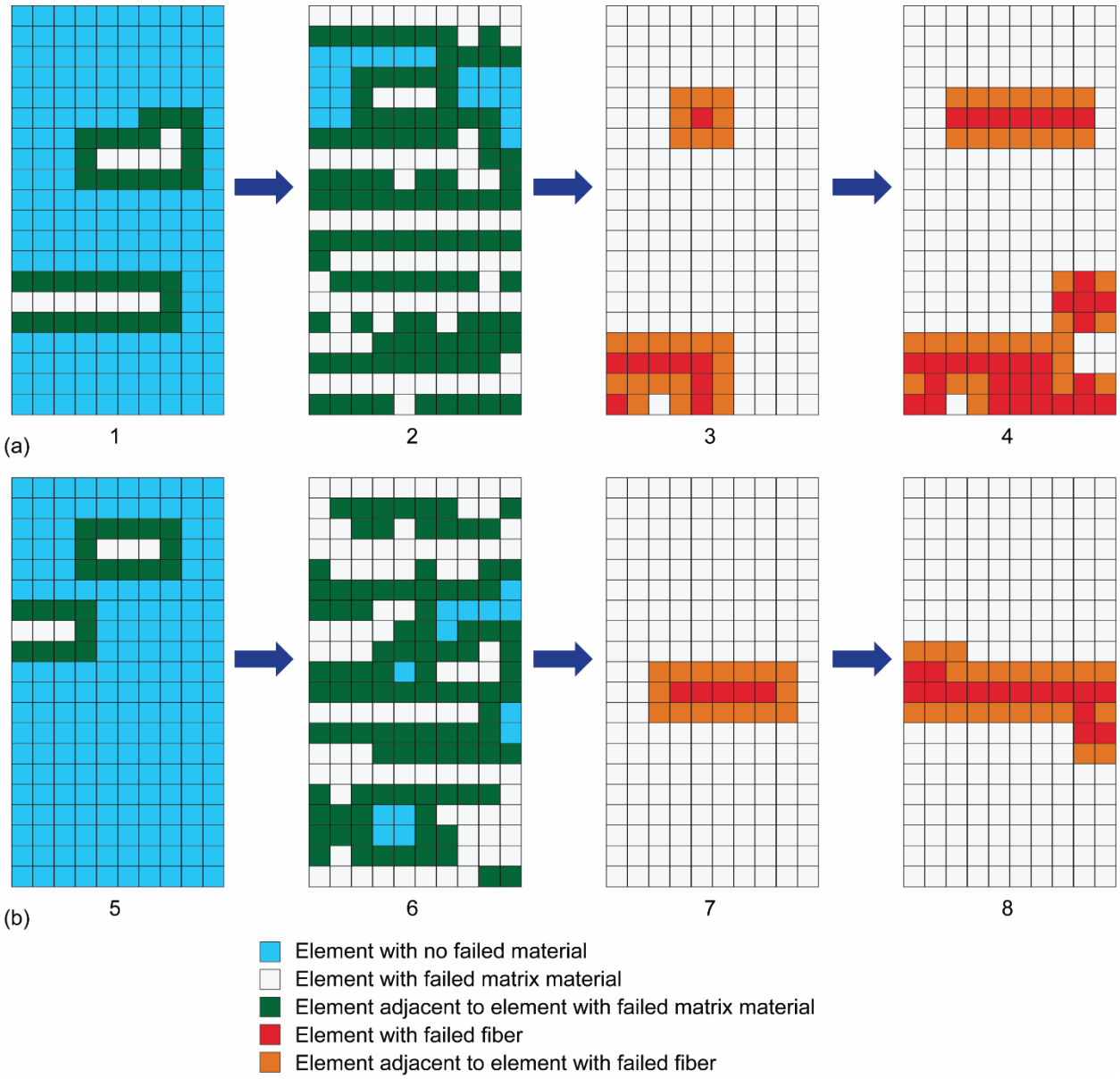

Figure 6.—Damage progression for two simulation trials ((a) and (b)) for the 0° tensile specimen with 30-vol% fibers. Damage progression is shown from left to right for early matrix damage, followed by the development of substantial matrix damage, followed by early fiber damage, followed by final composite failure. See Figure 4 for the coordinate system reference frame.

TABLE IV.—APPLIED STRAIN AND REACTION STRESS CORRESPONDING WITH FIGURE 6

Applied strain (Reaction stress, MPa)			
Early matrix damage	Substantial matrix damage	Early fiber failure	Final composite failure
Image from Figure 6			
1	2	3	4
0.001275 (232.3)	0.00162 (270.5)	0.00575 (473.9)	0.00615 (163.2)
5	6	7	8
0.001148 (216.5)	0.001735 (283.7)	0.00570 (587.0)	0.0060 (246.4)

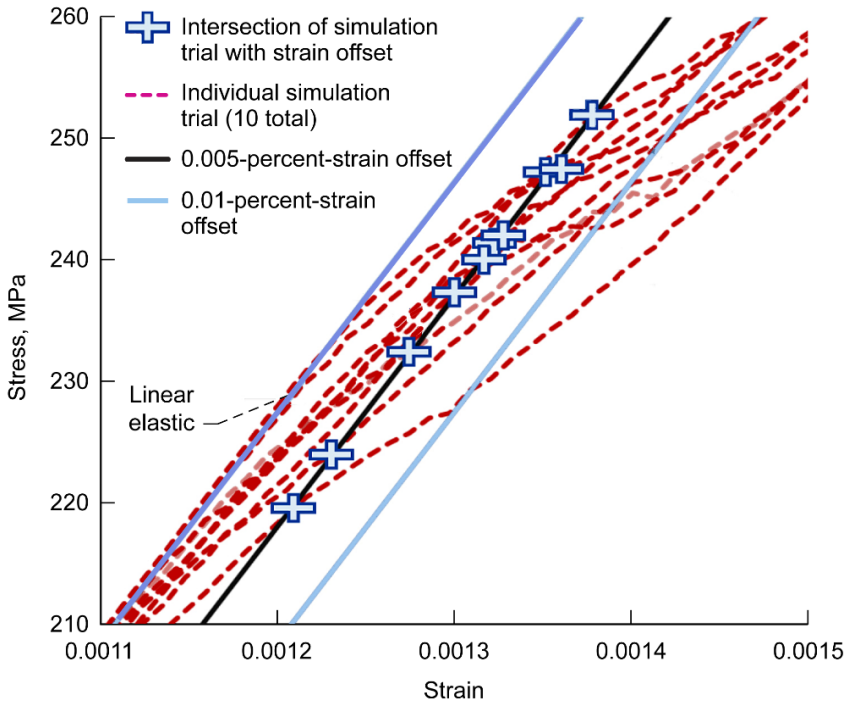

Figure 7.—Results from 10 simulation trials showing the stress-strain response between 0.0011 and 0.0015 strain for the 0° tensile specimen with 30-vol% fibers. The load step investigated the strain range between 0.0007 and 0.003 strain and was broken up into 200 loading increments of 0.0000115 strain. Also shown are the points where the simulations intersect a 0.005-percent-strain offset line.

The 10 intersection points in Figure 7 show the range of variability in the proportional limit stresses predicted by the simulations. By visually estimating the 10 stress values where the simulations intersected with the 0.005-percent-strain offset line, we obtained a mean of 238.2 MPa and a standard deviation of 10.3 MPa. This compares with the experimentally determined values of matrix cracking stress of 227 MPa and a standard deviation of 41 MPa (based on three or so specimens typically tested). The reported matrix cracking stress—the stress where the first matrix cracking was observed—does not correspond to a PLS-offset value, so the comparison between the simulation and experiment is only approximate. However, it is still an important outcome that FEAMAC/CARES can simulate some of the variability (scatter) in proportional limit stress. For actual CMCs, it is likely that other stochastic factors also play an important part in the scatter observed in proportional limit stress. Factors such as nonuniform fiber volume fraction, misalignment of fibers, and fibers in close proximity or touching one another are not considered in the simulations even though they will contribute additional scatter in measured proportional limit stresses.

3.3 Specimen With 90°-Oriented Fibers

We calibrated our model parameters to the 0° unidirectional CMC in tension. In this case, additional calibration or adjustment of our model was not necessary to match the strength response of the 90°-oriented fiber configuration in transverse tension. If it had been required, then additional model parameters that describe the transversely isotropic (anisotropic) strength response of the individual material constituents could have been used. This was done in Nemeth (2014), where these additional parameters were needed for the matrix material of a polymer matrix composite (PMC) to match to the experimentally measured strength of a unidirectional fiber-reinforced PMC loaded in transverse tension. Following this calibration process for the 0°- and the 90°-oriented tensile specimens, predictions and comparisons to other loading configurations and composite architectures could be made. In this case we

did not need to invoke (use) these additional model parameters. Therefore, the individual material constituents of the CMC were assumed to have isotropic strength behavior, and only the Weibull stochastic strength parameters listed in Table II were used in all subsequent damage response simulations.

In the technical paper describing the FEAMAC/CARES software (Nemeth et al., 2016), one section describes the response of a unidirectional fiber-reinforced composite from transverse tensile loading (Sec. 4.3.2, Nemeth et al., 2016). It shows that a brittle failure mode of sudden catastrophic rupture, where the specimen breaks into two separate pieces, was obtained with FEAMAC/CARES. In the remainder of this section, we expand on this result by comparing our simulations to the experimental results obtained by Bhatt and Phillips (1990) for a SiC/RBSN tensile specimen with fibers oriented 90° to the loading direction (transverse tensile loading).

The FEAMAC/CARES simulations (of transverse tensile loading) were for the CMC configuration with 30-vol% fibers. In our simulations the same finite element model of the tensile specimen gauge area and the same MAC/GMC RUC architecture was used as shown in Figure 4. Only a single composite layer was modeled so as to reduce computational overhead and encourage more rapid through-the-thickness failure (more composite layers would slow damage propagation through the thickness—and the MAC/GMC and RUC used here did not explicitly model crack propagation through the composite layers). The transverse loading in the model was applied as follows: in the tensile loading portion of the simulations (after the initial thermal cooldown load step) the total amount of displacement (from three subsequent loading steps) applied at the top edge of the specimen was 0.02 mm for a strain of 0.0008. Table V provides the breakdown of the three sequential load steps of displacement showing the strain range of each load step, the number of displacement increments, and the displacement imposed per each increment for this specimen configuration.

Figure 8 shows the results of 10 FEAMAC/CARES simulations of the stress-strain response of a SiC/RBSN CMC specimen (with 30-vol% 90°-oriented fibers) under uniaxial tension (transverse tensile loading). The figure indicates that once damage initiates within a given simulation trial, a sudden and large dropoff in stiffness develops from failure of the matrix. This catastrophic, or brittle-like, failure behavior is consistent with what is typically observed from specimen rupture experiments of transversely loaded unidirectional CMCs and PMCs. Figure 8 shows that there is a large amount of scatter in the fracture strength of the CMC consistent with brittle material behavior and a material having a low Weibull modulus of $m_V = 5.0$ for the matrix material. Bhatt and Phillips (1990) reported that the measured fracture stress was 27±3 MPa—indicating that there was much less scatter in comparison to the simulations. However, Bhatt and Phillips (1990) typically tested three or so specimens per experiment—which means that the statistical confidence of the reported strength scatter of ±3 MPa was low.

Figure 8 shows that a downward stress jump occurred, followed by an increase in stress (with increasing strain) and a reduced slope, until the simulation ended. The stress never reached zero at the bottom of the first downward jog (for a given simulation), and after the jog it increased continually, although at a lower rate than the response of the undamaged specimen. In the experimental tests, once the interfacial failure occurred, the composite failed almost immediately (Bhatt and Phillips, 1990). Goldberg (2012) commented regarding the same [90] laminate (for an analysis using MAC/GMC and the same RUC as shown in Fig. 2) that, at the point of interfacial failure, the rows of subcells that included

TABLE V.—LOAD STEP DESCRIPTION FOR SIMULATIONS OF LAMINATE SPECIMENS WITH 30-vol% 90°-ORIENTED FIBERS
[Total imposed displacement, 0.02 mm for 0.0008 strain.]

Stress-strain curve region	Total displacement and strain	Strain range	Number of displacement increments	Displacement per increment, mm
First stage (load step 2)— Elastic response and no damage	0.005 mm for 0.0002 strain	0.0 to 0.0002	10	0.0005
Second stage (load step 3)— Matrix cracking	0.0125 mm for 0.0005 strain	0.0002 to 0.0005	200	.0000375
Third stage (load step 4)— Fiber controlled until ultimate failure	0.02 mm for 0.0008 strain	0.0005 to 0.0008	100	.000075

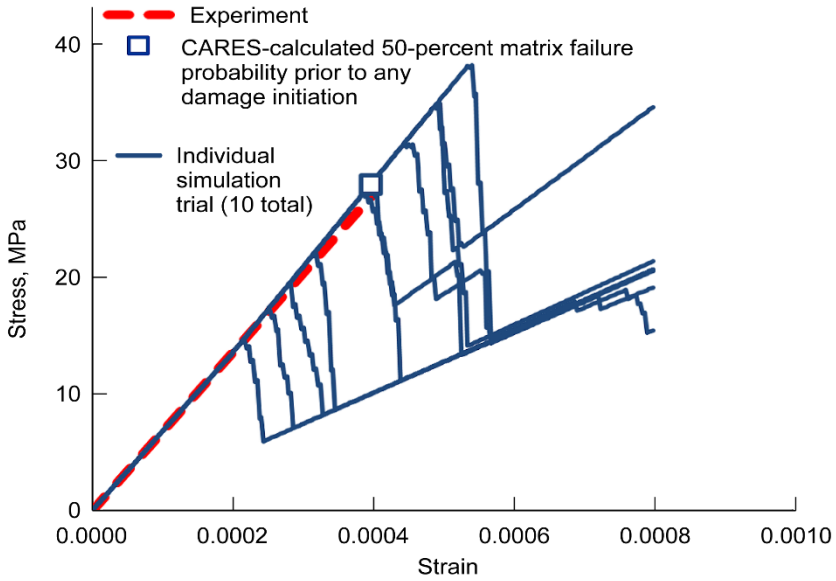

Figure 8.—Results of 10 simulation trials for the transversely loaded, unidirectional specimen compared with experimental data. Also shown is a 50-percent probability-of-failure data point obtained from one of the simulation trials prior to any damage initiation event.

the interface were assigned a reduced stiffness and could then carry a negligible amount of stress. However, the row of subcells consisting of pure matrix still was able to carry stress after the interfacial failure, as reflected in the increasing stress with strain in the stress-strain curve. This was confirmed by examining the secondary slope of the stress-strain curve (following the first downward jog), which was equal to the matrix modulus scaled by the volume percentage of the matrix-only row of the unit cell. The subsequent load-carrying capability is a numerical artifact. In an actual CMC, once the interfacial failure occurs, stress concentrations most likely form and cracks propagate, leading to a sudden brittle failure. Explicit crack propagation within individual material constituents and bimaterial interfaces is not modeled in the version of MAC/GMC used here.

Figure 8 shows good correlation with the experimental data for stress-strain response and fracture strength. This is noteworthy because the matrix material was assumed to have an isotropic strength response. However, this good correlation has to be viewed with some caution. Response of the material constituent is often anisotropic because of material morphology. It may also appear to be anisotropic because of inconsistencies or shortcomings in modeling. For that situation the material failure response has to be calibrated to the experimental data. The values used to control this model are parameters, but they also have a physical meaning or tie-in. There are inherent inaccuracies and/or compromises in the modeling (see for example section 4.1 of Nemeth et al. (2016)). These inaccuracies include modeling square-shaped fibers, the fiber-packing arrangement (assuming that the CMC is described by a square-packed fiber arrangement versus some other packing arrangement—like hexagonal-packed), and the inaccuracy (and lack of fidelity) in the detailed stress fields of GMC in comparison to those of HFGMC and FEA methodologies. Additional uncertainties like fiber volume fraction, alignment of fibers, and porosity mean that the good correlation with the experimental data can also be regarded as having an element of coincidence. This same experiment with a different CMC material or modeling assumptions could just as likely not have correlated as well with the experimental data. In that case, adjustments to the model could be necessary, such as allowing the matrix material to be anisotropic in strength response. That also could represent the true physical situation of the CMC material morphology. Therefore the good correlation shown to the experimental data in Figure 8 cannot be considered as a true validation of the model. Ultimately, the material failure response should be calibrated to the experimental data in this situation. This was done in Nemeth (2014), where the matrix material of a PMC was assumed to be

transversely isotropic (a form of anisotropy) in order to correlate with the available experimental data. We began this exercise by calibrating our model to data for a 0° unidirectional fiber CMC in tension; however, our model also has to be calibrated to the 90°-oriented-fiber configuration in transverse tension. Following that, predictions and comparisons to other loading configurations and composite architectures can be made more accurately.

Figure 8 shows that the transversely loaded unidirectional CMC is much weaker than the longitudinally loaded unidirectional CMC as shown Figure 5—a trend consistent with the experimental results shown in Figure 1. Figure 8 also shows the point where there is 50-percent probability of matrix failure of the entire specimen prior to a first damage initiation event. When damage initiates, it propagates rapidly—indicating brittle behavior. Figure 9 supports this with the results of 10 separate simulation trials, showing the final damage path of failed matrix material. Figure 9 shows that the failure path is often a single row of elements that traverse the specimen width where the matrix failed, as in the case of trials 4, 5, 6, and 9. For the other trials, the failure path involves only a couple or a few rows of elements traversing the specimen width, and those rows of elements are always in close proximity to one another.

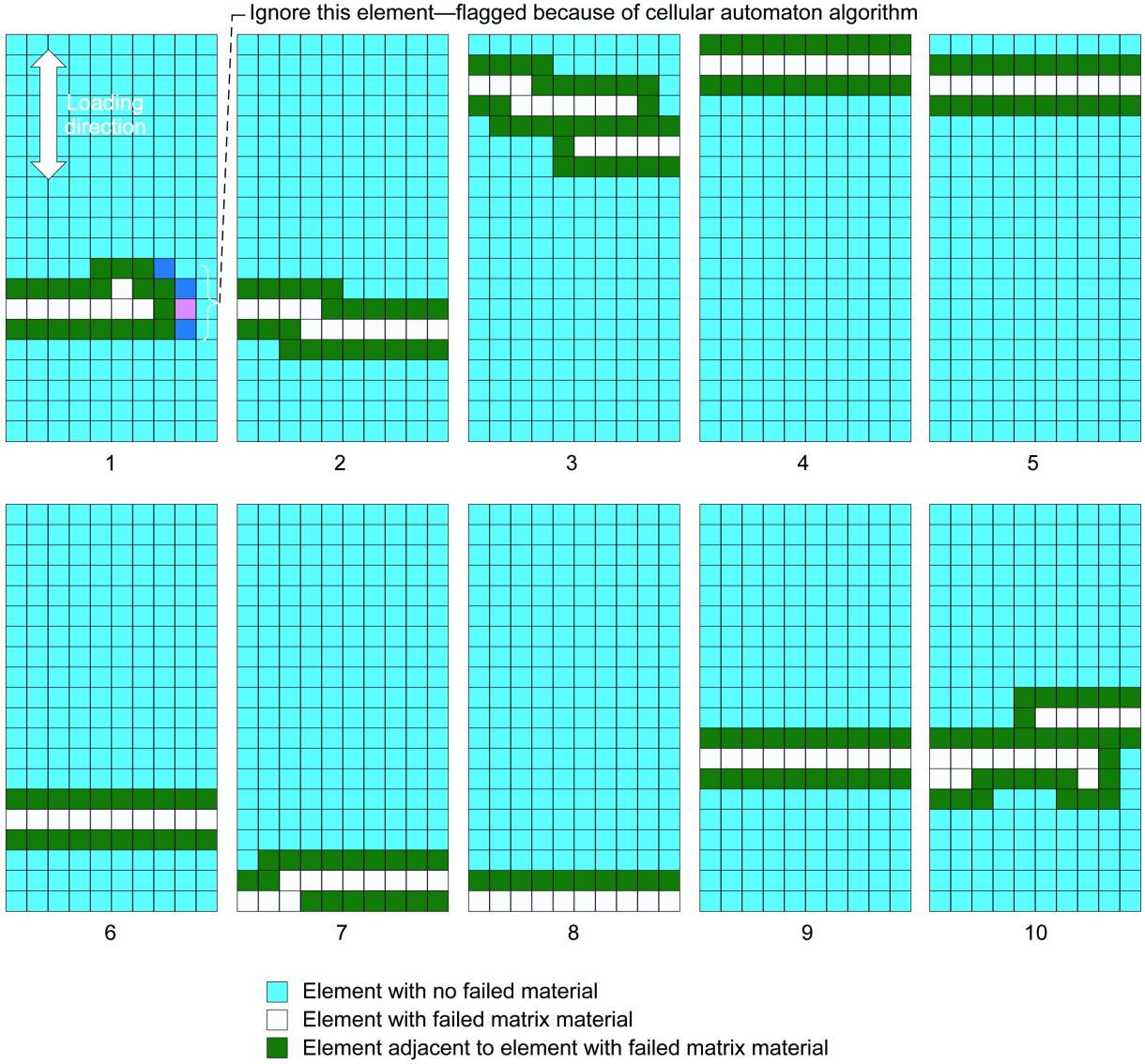

Figure 9.—Results of 10 simulation trials showing the final damage path of failed matrix material. The global coordinate system is shown in Figure 4; however, the fiber direction is 90° clockwise to that shown in Figure 4 and is parallel to the global x_1 direction.

4.0 Predictions for Off-Axis and Angled-Ply Laminate Configurations

4.1 Off-Axis Loading of Unidirectional Plies

Bhatt and Phillips (1990) tested eight-ply unidirectional laminates in tension with the fibers tilted at angles of 10° and 45° relative to the direction of loading ($[10]_8$ and $[45]_8$ off-axis-loaded tensile specimens). Figure 1 shows these results schematically. The finite element model shown in Figure 4 was used, but the material coordinate system was redefined to reflect the ply layup appropriately.

The off-axis laminates deform nonsymmetrically during cooldown from the stress-free temperature, and this needs to be considered in the model. For the 0° and 90° unidirectional laminates, the specimens should have contracted symmetrically from their stress-free temperatures as they cooled—therefore maintaining an overall rectangular shape. That is not the case for the off-axis unidirectional laminates. For those laminates, the cooldown causes the specimens to deform to a parallelogram (although the amount of distortion from the rectangular shape to the parallelogram shape would be very small). We allowed for this nonsymmetrical contraction in our Abaqus model. We also subsequently examined the effect of additional nodal constraints at the grip ends of the specimen when a fixed displacement ramp load was applied. This added constraint was done to simulate a rigid loading fixture (that would not allow lateral movement of the specimen), whereby the specimen would remain aligned with the testing fixture load axis as the displacement load was applied.

In reality, the off-axis laminate specimens that would be cut from a prepared CMC panel (that had already gone through the thermal cooldown) would not have any shape distortion of the type just described (the specimen cut from the panel would be rectangular). However, it is difficult to capture this in the finite element model while accounting for the residual stresses that build up in the individual material constituents from the thermal cooldown process.

The Abaqus input deck (input file: *.inp) that was constructed for the 0° and 45° off-axis loading of unidirectional laminates consisted of two separate, but sequential, loading conditions (steps), where the results from the previous loading condition were used as the initial condition for the subsequent loading condition. The first condition (load step 1) was the thermal cooldown from the initial stress-free temperature in order to impart residual stresses on the individual material constituents. This was done over the course of several time increments (arbitrarily set as 10 equally spaced increments that cooled the specimen from 550 °C to a room temperature of 23 °C. This was imparted as a “ramp” load. For the off-axis loaded unidirectional plies, this distorted the originally rectangular shape of the specimen to a parallelogram (the specimen, however, did not warp and remained flat). A single node along the bottom specimen edge at the midpoint (or nearest node) along the edge was fixed for the three displacement directions (1, 2, and 3 for the global coordinate system reference frame shown in Fig. 4) and one rotational degree of freedom (5). A single node along the top specimen edge approximately at the midpoint along the edge was fixed for the displacement directions (1 and 3) and one rotational degree of freedom (5). These boundary conditions allowed the specimen to freely contract as the temperature lowered while also preventing rigid-body modes.

The results from the thermal cooldown load step were used as the initial starting condition for the next loading sequence (load step 2). This loading sequence imparted a ramp displacement (in direction 2) along the top edge of the specimen consistent with uniaxial loading of a tensile specimen. Load step 2 was applied over 250 equally spaced displacement increments. This load condition sequence traversed the stress-strain curve to some point past complete matrix failure. However, in this case the boundary of the bottom edge was fixed (using the BOUNDARY, FIXED keyword in the Abaqus input file) in direction 2—the direction of loading. This restrained the bottom edge from any further displacement in direction 2 while maintaining the distortion of the bottom edge from the thermal cooldown load step. This potentially overconstrained our model from the subsequent ramp displacement loadings because Poisson contraction effects were no longer orthogonal to the loading direction. However, examination of the stresses that developed showed no stress concentration effects (the stresses were completely uniform throughout the specimen) prior to any damage initiation event.

To investigate further we subsequently changed our finite element model so that the specimen behaved as though it was held in a rigid fixture that did not allow drift (side-to-side movement). In other words the load fixture could only move in direction 2, and it maintained alignment while the displacement was applied. To do this we constrained the movement of two nodes in direction 1—one at the top edge of the specimen and one at the bottom edge of the specimen approximately midway along the specimen width (the bottom edge node was also constrained in directions 2 and 3 to rigidly fix the node and prevent rigid-body modes). This constraint caused stress concentrations to develop in the specimen, an example of which is shown in Figure 10. However, the effect of this constraint on the overall damage response of the specimen was relatively negligible, as will be shown subsequently. In Bhatt and Phillips (1990), there is no mention of any effect from the grip fixturing on the damage response of the specimen.

Figure 10(a) shows results for σ_{11} stresses just prior to a first damage event for a 10° off-axis load. The effect of the two nodes constrained at the top edge and bottom edge in the middle of the specimen can be seen. Figure 10(b) shows the σ_{22} stress distribution just prior to this first damage event for the 10° off-axis load. Because the shape of the specimen was no longer rectangular after the thermal cooldown, the imposed displacement load could not be applied uniformly to the top edge, but rather displacement had to be applied to the individual nodes along the top edge. The nodal displacements were applied so that a uniform level of strain was imposed along the top edge of the specimen.

Figure 11 shows results of 20 simulation trials compared with experimental data. Of the 20 trials shown, 10 simulate specimens with a rigid fixture and 10 simulate specimens without rigid support. Also shown is a 50-percent probability-of-failure data point obtained from one of the simulation trials prior to any damage initiation event. Figure 11 shows that, with or without the two nodes constrained to imitate a rigid loading fixture, the point of initiation of damage appears to be about the same. Only as damage develops is there a noticeable change in the stress-strain response. Without the additional constraint, damage develops more rapidly or is more brittle-like. With the additional constraint, damage growth appears to be more gradual as strain is increased. Bhatt and Phillips (1990) reported a more brittle-like failure mode for this specimen configuration; however, without more information regarding details of the experimental results, it is not clear which of the two modeling options better represents the true behavior of the particular specimen configuration.

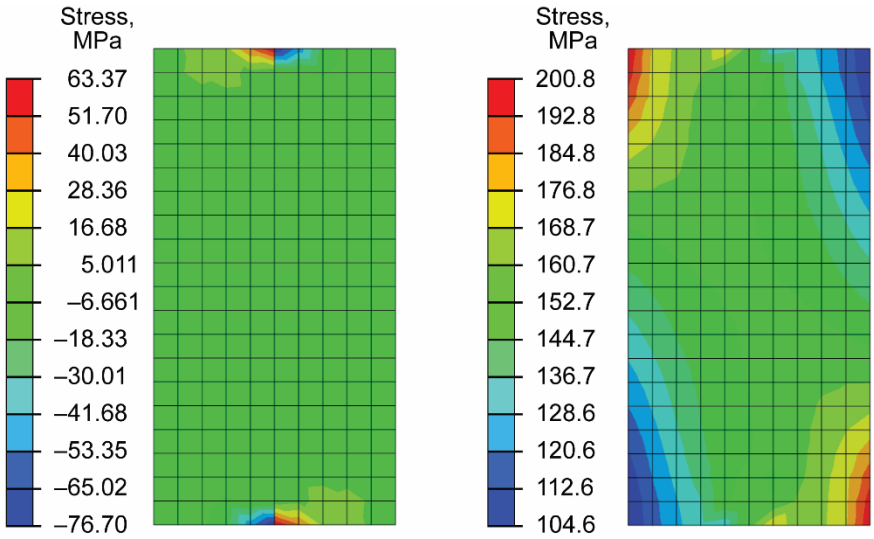

Figure 10.—Example of stress concentrations that develop in the 10°-off-axis specimen when a displacement load is applied in direction 2 (the loading direction). The global coordinate system is shown in Figure 4, however, the fiber direction is 10° clockwise to that shown in Figure 4. (a) σ_{11} stress distribution. (b) σ_{22} stress distribution.

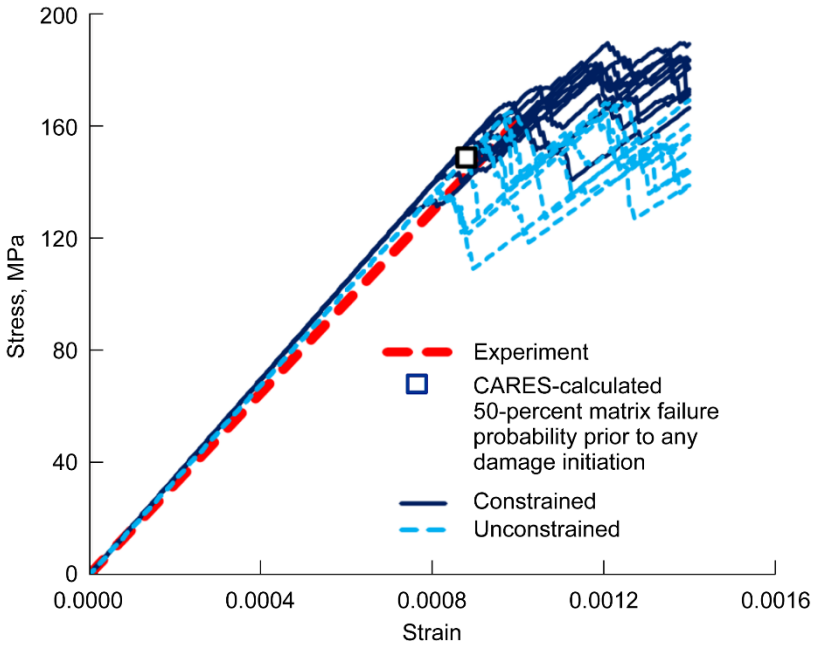

Figure 11.—Results of 20 simulation trials for the 10°-off-axis unidirectional specimen compared with the experimental data. Of the 20 trials shown, 10 simulate specimens with a rigid fixture and 10 simulate specimens without rigid support. Also shown is a 50-percent probability-of-failure data point obtained from one of the simulation trials prior to any damage initiation event.

Figure 12 shows results of 10 separate simulation trials modeling the rigid support, showing early and final damage paths of failed matrix material for the 10°-off-axis unidirectional loaded tensile specimen. These results are shown as deformed plots with exaggerated scale. The deformed plots provide a sense of how the off-axis fiber orientation influences the development of damage and how it tends to deform the CMC to be askew (or tries to crease it). Figure 12 shows that the two nodes that were constrained to prevent lateral (side-to-side) movement of the specimen sometimes showed early matrix failure at these points. This can be seen in simulations 1, 2, and 3 in Figure 12. The fact that this occurrence was in the first three simulations and not in the subsequent simulations appears to be a coincidence. The damage did not propagate from these constrained points as the simulations progressed through the load steps (probably because the stresses were relaxed at these points when the matrix failed). The damage at these nodes was somewhat isolated (happening in 3 of 10 simulation cases), and the effect of constraining these nodes had some influence, but it did not greatly affect the stress-strain damage response of the specimen (as shown in Fig. 11). Therefore we believe that the introduction of constraint at these nodes to resist lateral movement (imitating a rigid load frame fixture) was an acceptable approach to model the effect of a stiff load frame and that this did not greatly interfere with the progressive damage development within the specimen gauge section.

Figure 13 shows the results of 20 simulation trials compared with experimental data for the 45°-off-axis-loaded unidirectional laminate. Of the 20 trials shown, 10 simulate specimens with a rigid fixture and 10 simulate specimens without rigid support. Also shown is a 50-percent probability-of-failure data point obtained from one of the simulation trials prior to any damage initiation event. Figure 13 shows that, with or without the two nodes constrained to imitate a rigid loading fixture, the average point of initiation of damage appears to be about the same. Unlike in Figure 11 there is no noticeable difference in the stress-strain response from the constrained-node response and the unconstrained-node response. In each simulation the damage rapidly developed in a brittle-like manner with a sudden dropoff in stress at some point in the applied strain. There was also a great deal of scatter in the level of stress at the point where damage initiated in the individual simulations. Again, this is consistent with brittle material behavior. Bhatt and Phillips (1990) also observed a brittle-like failure mode for this specimen configuration.

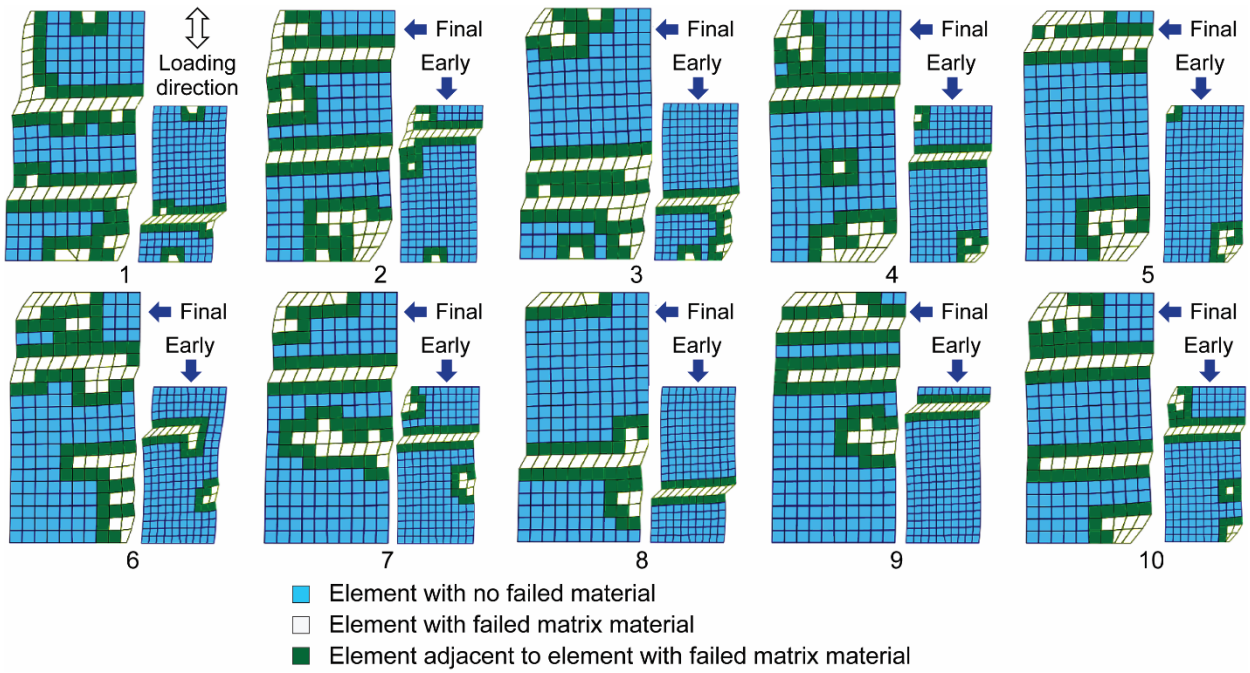

Figure 12.—Results of 10 simulation trials modeling the rigid support showing the early and final damage paths of failed matrix material for the 10° off-axis unidirectionally loaded tensile specimen. These are deformed plots with exaggerated scale.

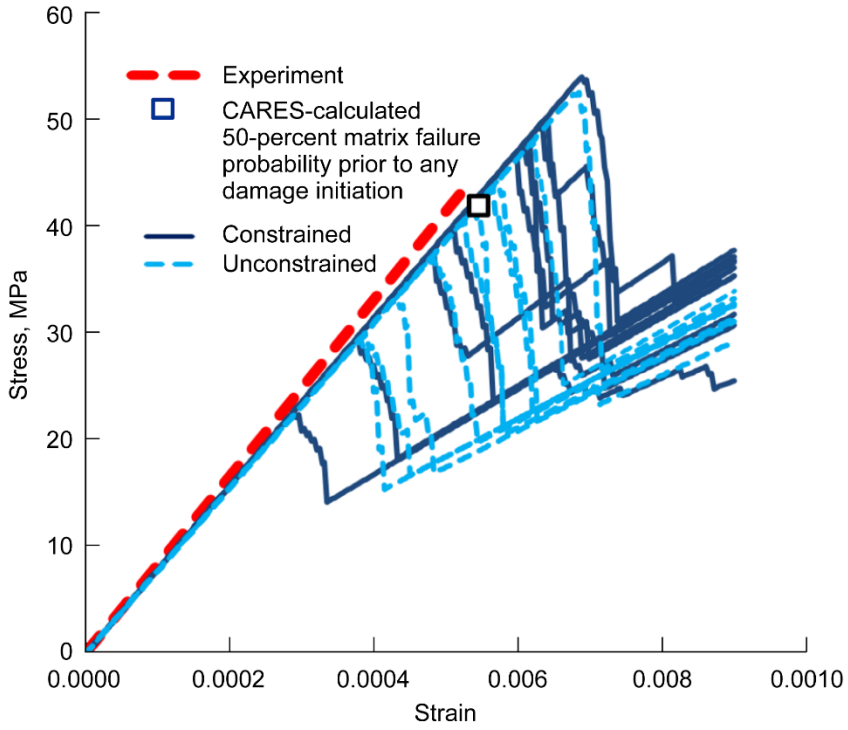

Figure 13.—Results of 20 simulation trials for the 45° off-axis unidirectional specimen compared with experimental data. Of the 20 trials shown, 10 simulate specimens with a rigid fixture and 10 simulate specimens without rigid support. Also shown is a 50-percent probability-of-failure data point obtained from one of the simulation trials prior to any damage initiation event.

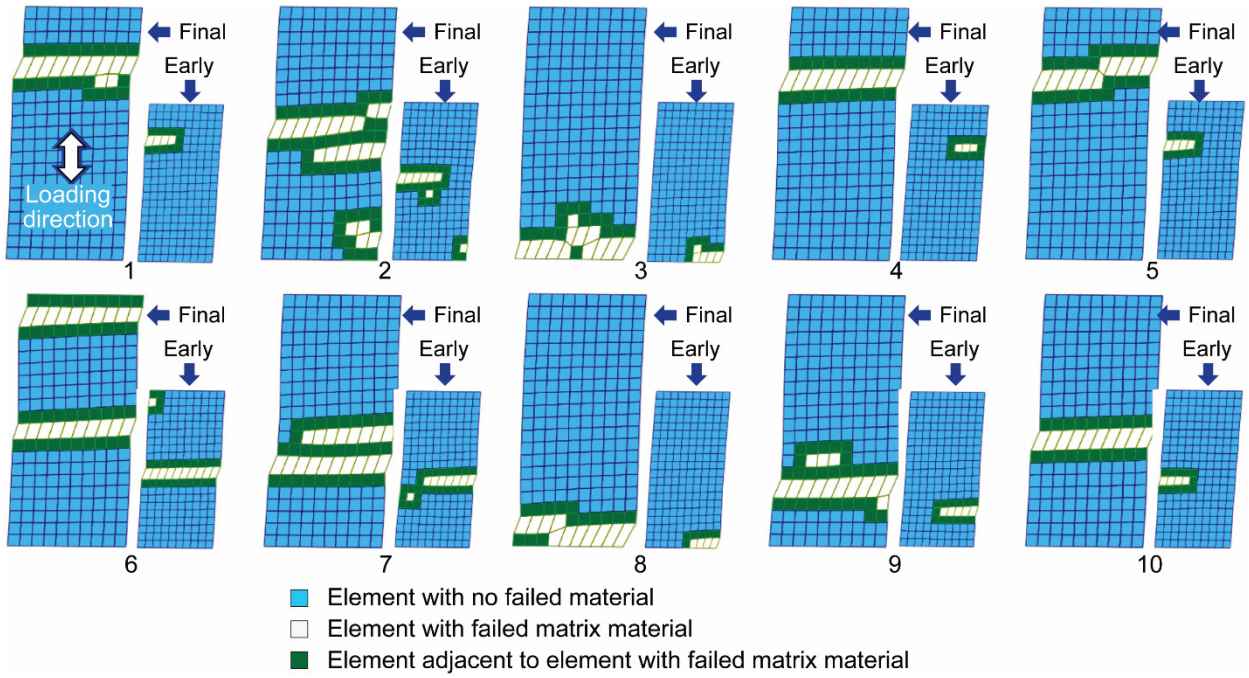

Figure 14.—Results of 10 simulation trials modeling rigid support for 45°-off-axis unidirectionally loaded tensile specimens and showing the early and final damage paths of failed matrix material. These are deformed plots with exaggerated scale. The fiber direction is 45° clockwise to that shown in Figure 4.

Figure 14 provides results of 10 simulation trials modeling rigid support, showing early and final damage paths of failed matrix material for the 45°-off-axis unidirectionally loaded tensile specimen. These are deformed plots with exaggerated scale. Unlike Figure 12 for the 10°-off-axis-loaded specimen, Figure 14 for the 45°-off-axis-loaded unidirectional specimen did not show any matrix failures at the two nodes that were constrained to prevent lateral (side-to-side) specimen movement. Also unlike Figure 12, Figure 14 tends to show that matrix failure developed perpendicular to the loading direction and that fewer rows of elements, often only a single row or two rows of damaged elements, developed. This is also strongly indicative of brittle material behavior. Bhatt and Phillips (1990) indicated that off-axis laminates typically fractured in a brittle manner; however, it is not clear that the results in Figure 14 adequately capture the details of the progression of damage until final specimen failure (compare with Fig. 7 in Bhatt and Phillips, 1990).

4.2 0/90 and +45/–45 laminates

Bhatt and Phillips (1990) also tested cross-ply ($[0_2/90_2]_s$) and angled-ply ($[+45_2/-45_2]_s$) laminates in tension, and these results are shown schematically in Figure 1. The $[0_2/90_2]_s$ stress-strain response displayed bilinear behavior having an initial linear-elastic response for the undamaged material at low load levels. At higher load levels matrix cracking began and eventually saturated the CMC with a regular pattern of crack spacing. The $[+45_2/-45_2]_s$ stress-strain curve displayed an initial elastic response followed by matrix damage and a more gradual softening of the stress-strain curve. For the cross-ply laminate simulations we used the same finite element model of the tensile specimen gauge area and MAC/GMC RUC as were used for the unidirectional laminate simulations (shown in Fig. 4). However, instead of modeling only a single ply as was done in the simulations of the unidirectional laminates, the cross-ply laminates were each modeled with four plies—arranged in separate $[0/90]_s$ and $[+45/-45]_s$ configurations. We did this because the CMC could be equivalently considered as consisting of four layers of unidirectional plies. Modeling only four plies considerably reduced the computational overhead in comparison to

simulating the full eight plies, and it also encouraged a more rapid through-the-thickness failure (more composite layers slowed damage propagation through the thickness).

The tested cross-ply laminate configurations had fiber orientations that were symmetrical relative to the loading direction. Therefore the CMC maintained an overall rectangular shape after the thermal cooldown load step. The boundary conditions chosen are therefore the same as those for the 0° and 90° laminates previously described.

4.2.1 $[0/90]_s$ Laminate Simulations

The input for the $[0/90]_s$ laminate consists of four separate load steps encompassing the cooldown phase from the stress-free temperature followed by three load steps that put sequential displacements on the top of the specimen in the direction oriented perpendicular to that top edge. Figure 15 shows a set of results for 10 simulations for the $[0/90]_s$ laminate tensile specimen with 30 vol% fibers. In the tensile loading portion of the simulations (after the initial thermal cooldown load step) the total displacement (from the subsequent three loading steps) at the top edge of the specimen was 0.2 mm for a strain of 0.008. Table VI provides the breakdown of the three sequential load steps of displacement, showing the strain range of each load step, the number of displacement increments, and the displacement imposed per each increment for this specimen volume fraction.

In Figure 15 the stress-strain curves for the 10 simulations for the $[0/90]_s$ laminate configuration matched the experimental data from Bhatt and Phillips (1990) reasonably well. The 10 simulations showed similar behavior, with little variation from one simulation to another (at the scale shown) except at the highest stresses where fiber failure was occurring. This is consistent with the results from the 0° unidirectional-ply simulations in Figure 5, where little variation from one simulation to another was apparent at the scale shown. The “graceful failure” behavior in the nonlinear portion of the stress-strain curve (approximately between 0.001 and 0.004 strain) where matrix cracking occurred was appropriately reproduced in the simulations. The point where matrix cracking began to become apparent (shown as deviation from the linear-elastic portion of the stress-strain curve for the undamaged material) visibly matched well with the experimental data. The experimental results curve was a bilinear line reproduced

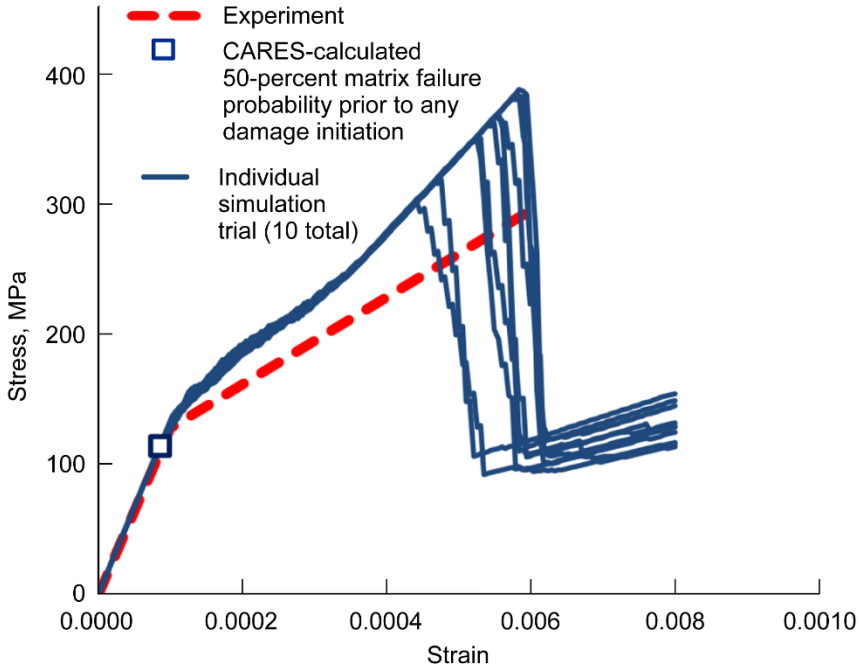

Figure 15.—Results of 10 simulation trials for the $[0/90]_s$ specimen compared with experimental data. Also shown is a 50-percent probability-of-failure data point obtained from one of the simulation trials prior to any damage initiation event.

TABLE VI.—LOAD STEP DESCRIPTION FOR SIMULATION OF SPECIMENS WITH LAMINATE CONFIGURATION OF 30-vol% $[0/90]_S$ FIBERS
[Total imposed displacement, 0.2 mm for 0.008 strain.]

Stress-strain curve region	Total displacement and strain	Strain range	Number of displacement increments	Displacement per increment, mm
First stage (load step 2)— Elastic response and no damage	0.015 mm for 0.0006 strain	0.0 to 0.0006	10	0.0015
Second stage (load step 3)— Matrix cracking	0.0775 mm for 0.0031 strain	0.0006 to 0.0031	200	.0003125
Third stage (load step 4)— Fiber controlled until ultimate failure	0.2 mm for 0.008 strain	0.0031 to 0.008	100	.001225

from Bhatt and Phillips (1990) as previously mentioned, and the actual stress-strain curves of the individual specimens were not recorded. Therefore the experimental results curve shown in Figure 15 is only an approximation of the actual behavior. In that light, the fit to the experimental data is quite acceptable, particularly at the "knee" in the curve where matrix microcracking was initiating (between approximately 0.0008 and 0.001 strain). Bhatt and Phillips (1990) reported that matrix fracture strength was 127±26 MPa and the ultimate strength was 294±87 MPa. In the fiber-controlled portion of the stress-strain response (starting at approximately 0.004 strain and continuing until fiber fracture) the effect of matrix fragments (the fragments of matrix still attached to fibers) on the stress-strain response was not considered. That region of the stress-strain curve was controlled only by the response of bare fibers in our modeling scheme. This would explain the deviation of the stress-strain response from the experimental data curve starting at about 0.004 strain and higher. Also shown in Figure 15 at about 0.0008 strain is the CARES/*Life*-calculated 50-percent probability of matrix failure of the whole tensile specimen prior to the first damage initiation event. Plots of damage progression (like Fig. 6) are not shown here but would appear similar to Figure 6. This version of FEAMAC/CARES was not capable of examining layer-by-layer damage progression in multilayer laminates when a single layer of shell elements was used to model a structure.

Figure 16 shows a closeup of the stress-strain response between 0.00085 and 0.00125 strain in order to highlight the stochastic behavior. For these simulations, we investigated the strain range between 0.0006 and 0.0031 strain in 200 loading increments of 0.0000125 strain. The variation in the stress-strain behavior from one simulation to another is now evident. Figure 16 shows three lines. One line is an extrapolation of the linear-elastic behavior of the CMC prior to any damage initiation event. The second line shows this same linear-elastic behavior line offset by 0.00005 strain (0.005-percent-strain offset), and the third line shows this same linear-elastic behavior line offset by 0.00010 strain (0.01-percent-strain offset). The second line (the 0.005-percent-strain offset) is the PLS-offset line. The figure shows where each simulation trial intersects this line. The 10 intersection points show the range of variability in the stress predicted by the simulations. We visually estimated the 10 stress values where the simulation intersected with the 0.005-percent-strain offset, obtaining a mean stress of 133.3 MPa and a standard deviation of 8.1 MPa. The experimentally determined values for matrix cracking stress of 127 MPa with a standard deviation of 26 MPa (based on three or so specimens typically tested). The literature-reported matrix-cracking stress was the stress where the first matrix cracking was observed and does not correspond to a proportional-limit strain-offset value. So the results between the simulation and experiment cannot be rigorously compared.

4.2.2 $[+45/–45]_s$ Laminate Simulations

The input for the $[+45/–45]_s$ laminate consists of four separate load steps encompassing the cooldown phase from the stress-free temperature followed by three load steps that put sequential displacements on the top of the specimen in the direction oriented perpendicular to that top edge. In the tensile loading portion of the simulations (after the initial thermal cooldown load step) the maximum total amount of

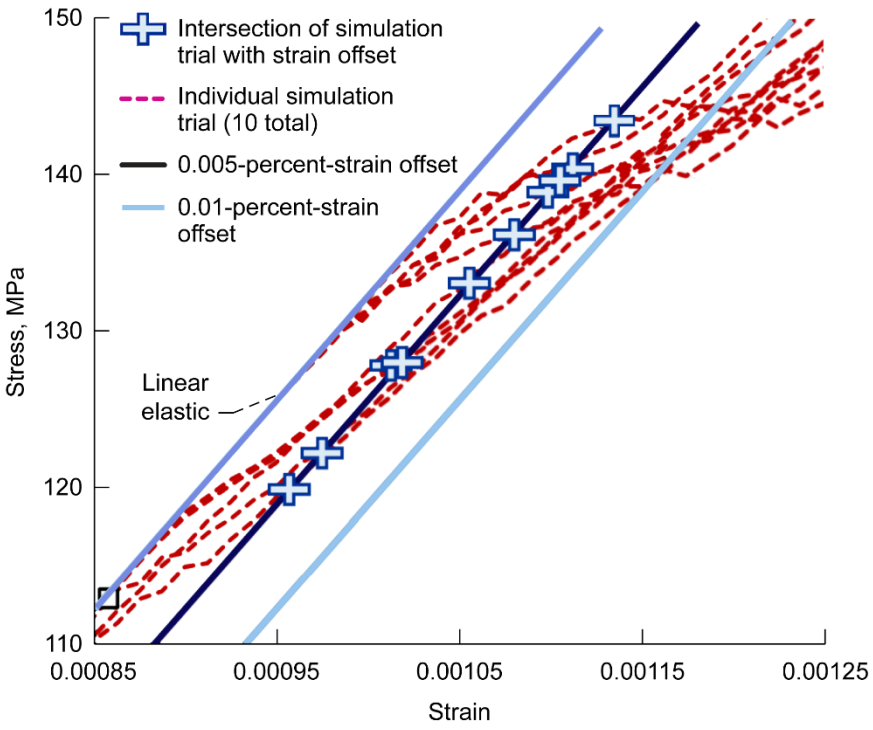

Figure 16.—Results from 10 simulation trials showing the stress-strain response between 0.00085 and 0.00125 strain for the $[0/90]_s$ laminate. The load step investigated the strain range between 0.0006 strain and 0.0031 strain and was broken into 200 loading increments of 0.0000125 strain. Also shown are the CARES 50-percent probability of failure and the points where the simulations intersect a 0.005-percent-strain offset line.

TABLE VII.—LOAD STEP DESCRIPTION FOR SIMULATION OF SPECIMENS WITH 30-vol% FIBERS AND LAMINATE CONFIGURATION OF $[+45/-45]_S$
[Total imposed displacement, 0.05 mm for 0.002 strain.]

Stress-strain curve region	Total displacement and strain	Strain range	Number of displacement increments	Displacement per increment, mm
First stage (load step 2)— Elastic response and no damage	0.015 mm for 0.0006 strain	0.0 to 0.0006	10	0.0015
Second stage (load step 3)— Matrix cracking	0.0325 mm for 0.0013 strain	0.0006 to 0.0013	100	0.000175
Third stage (load step 4)— Fiber controlled until ultimate failure	0.05 mm for 0.002 strain	0.0013 to 0.002	100	0.000175

displacement (from the subsequent three loading steps) at the top edge of the specimen was 0.05 mm for a strain of 0.002. Table VII provides the breakdown of the three sequential load steps of displacement, showing the strain range of each load step, the number of displacement increments, and the displacement imposed per each increment for this specimen volume fraction.

Figure 17(a) shows results of 10 simulation trials compared with the experimental data for the $[+45/-45]_s$ unidirectional tensile specimen with 30-vol% fibers. Also shown in Figure 17(a) is a 50-percent probability-of-matrix-failure data point obtained from one of the simulation trials prior to any damage initiation event. Figure 17(b) shows a micrograph of the matrix cracking pattern, reproduced from

Bhatt and Phillips (1990), showing that the matrix microcracks that formed early were roughly perpendicular to the direction of loading. Figure 17(a) shows that the fracture behavior from one simulation to another can vary appreciably. Some of the simulations show a more dramatic (or steep) falloff of stress with increasing strain, and other simulations show a more gradual falloff of stress with increasing strain. All of the simulations show that some matrix damage events occur prior to any rapid dropoff of stress with strain. The overall behavior resembles the experimental behavior shown schematically in Figure 1, where a more gradual dropoff of stress with increasing strain is indicated. From Bhatt and Phillips (1990), the matrix fracture stress was 75±10 MPa and the ultimate strength was 88±16 MPa.

Figure 18 shows the results of the 10 simulation trials, showing the early and final damage paths of failed matrix material for the $[+45/–45]_s$ laminate uniaxially loaded tensile specimen. These are deformed plots with exaggerated scale. For simulation 10, the damage pattern at about the midpoint of the matrix damage development is also shown because that simulation had a complicated damage pattern. No fiber failure events occurred in any of the simulations. Figure 17(b) shows that the early matrix microcracking tended to develop perpendicular to the loading direction, and Figure 18 shows that early matrix failure paths tended to develop perpendicular to the loading direction in simulations 1, 2, 3, 6, 7, and 8. The simulations do not reproduce the crack densities that are actually observed. Rather, the simulations qualitatively reproduce some observed behaviors. Also, because the simulations are for a four-layer laminate, FEAMAC/CARES cannot show the layer-by-layer damage development for the shell elements. The matrix failure patterns shown in Figure 18 are results averaged through the layers.

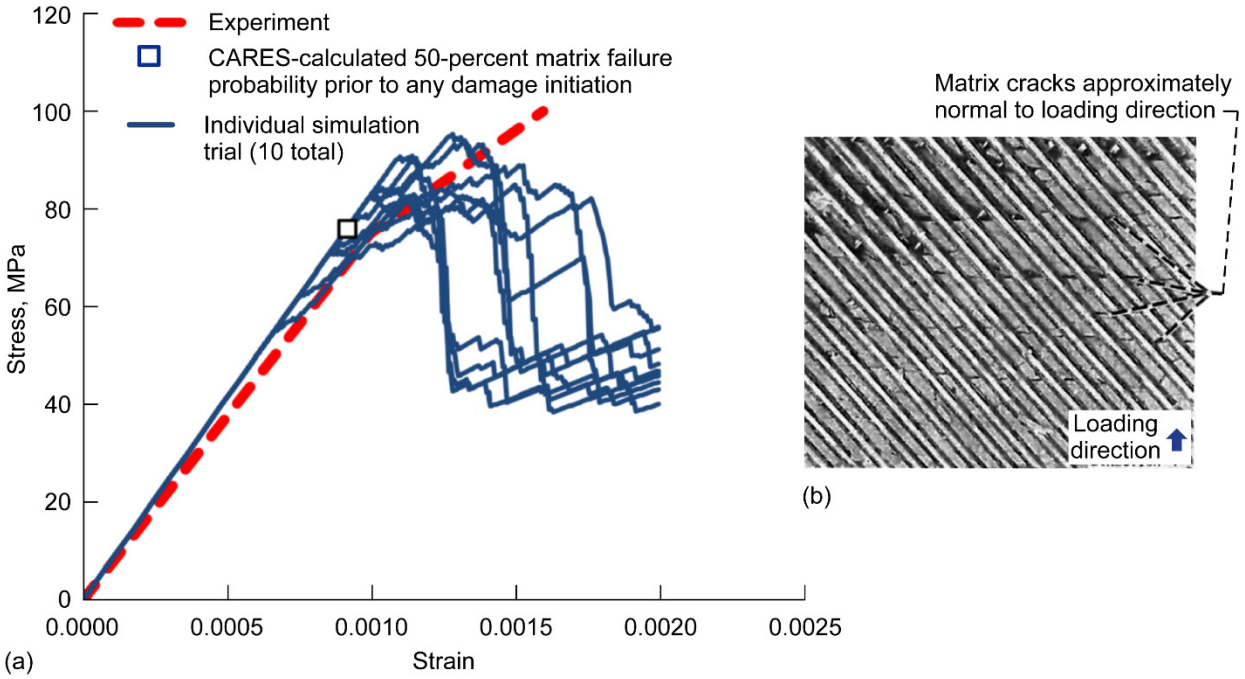

Figure 17.—Results and data for $[+45/–45]_s$ unidirectional tensile specimen. (a) Results of 10 simulation trials compared with experimental data (depicted here as a bilinear line until peak stress). Also shown is a 50-percent probability-of-failure data point obtained from one of the simulation trials prior to any damage initiation event. (b) Micrograph showing the matrix microcracking pattern. From Bhatt and Phillips, 1990. Copyright © 1990 ASTM International; used with permission.

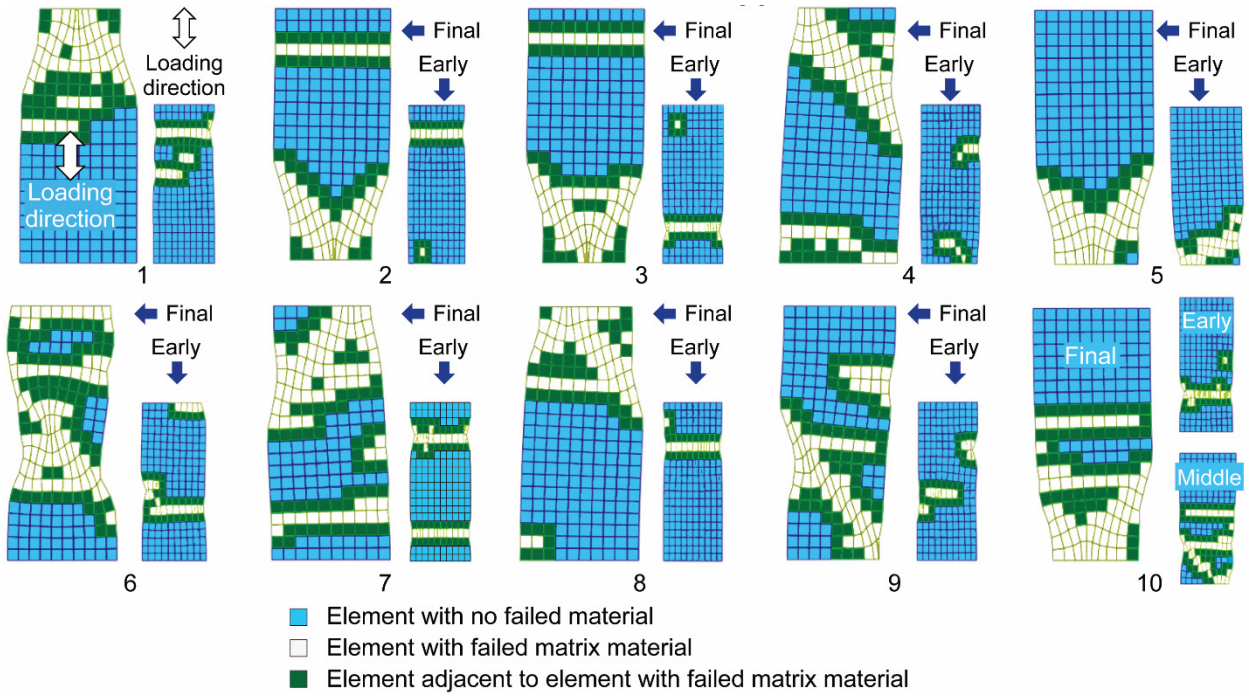

Figure 18.—Results of 10 separate simulation trials showing the early and final damage paths of failed matrix material for the $[+45/–45]_S$ laminate uniaxially loaded tensile specimen. These are deformed plots with exaggerated scale.

4.3 Double-Notched and Central-Hole Specimen Simulations

In this section we compare the strength of double-edge-notched 0° unidirectional tensile specimens simulated with FEAMAC/CARES with test results in Bhatt and Phillips (1990). We also show results of a simulation of a 0° unidirectional tensile specimen with a central hole. The central-hole configuration was not tested by Bhatt and Phillips, but it is included here so that the differences in the predicted failure modes can be compared for the two specimen configurations.

For the double-notched tensile specimen, 1-mm-wide notches were cut to a depth of 3.0 mm in the width direction and at the midsection of the specimen gauge section. The overall specimen gauge-section geometry remained the same (25 by 12.7 by 1.2 mm). The matrix fracture strength and the ultimate composite strength of the laminates were measured based on net cross-sectional area. The tested matrix cracking stress was 226±15 MPa, and the ultimate tensile strength was 650±135 MPa. The test results showed that the notches had no significant effect on the tensile properties of the $[0]_8$ laminates. To determine the mechanism of notch insensitivity, Bhatt and Phillips (1990) optically observed a double-notched tensile specimen during tension testing. Initially, for up to an average stress level of ~65 MPa (calculated from net cross-sectional area at the notches), the specimen showed no indication of damage. As the specimen was stressed beyond this level, cracks were formed at the notch tip along the fiber/matrix interface, which eventually resulted in axial splitting (parallel to the direction of loading) as opposed to the development of matrix cracking transverse to the direction of loading and located in the region between the notches (see Fig. 19). As the load increased, the axial splitting diminished or arrested and the notched specimen behaved in a manner similar to that of the unnotched specimen (development of matrix cracking transverse to the direction of loading and located in the region between the axial splits). Bhatt and Phillips (1990) concluded that crack blunting at the notch tip was probably the major reason for the insensitivity to the notches.

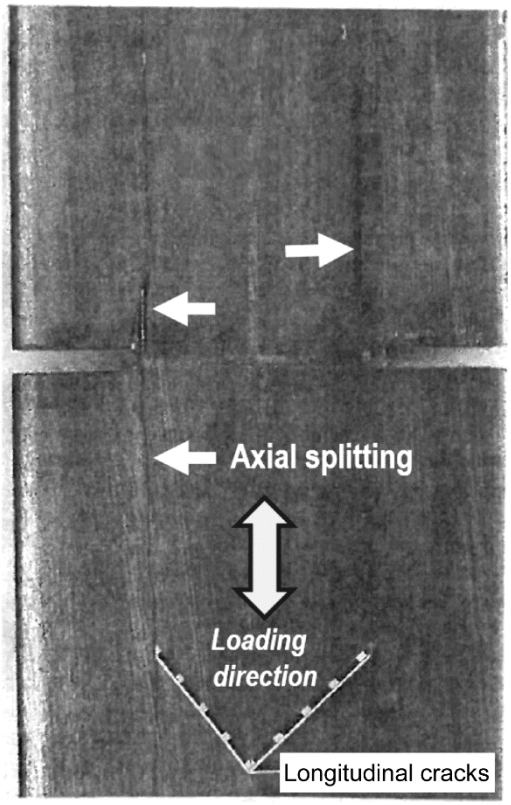

Figure 19.—Development of matrix cracks parallel to the direction of loading (axial splitting) from the tips of the notches during the early stages of loading for the $[0]_8$ experiment. From Bhatt and Phillips, 1990. Copyright © 1990 ASTM International; used with permission.

For the simulations, the double-notched and central-hole finite element models were prepared using Abaqus S4-type shell elements. Figures 20(a) and 20(b) show the generated meshes of the double-notched and central-hole specimens, respectively. These models are for the specimen gauge section used previously (25 by 12.7 by 1.2 mm). The dimensions for the double-notch mesh were the same as that used by Bhatt and Phillips (1990), and the diameter of the hole was arbitrarily made to be 4.0 mm—approximately one-third of the width of the specimen. The size of hole was chosen so that specimen edge had little influence on the stress field nearer to the edge of the hole. In both models in Figure 20, the meshes were refined (the element density was increased) at the regions where stress concentrations would occur.

The same RUC as shown in Figure 4 was used here for the FEAMAC/CARES simulations of the double-notch and central-hole specimens. Only a single composite layer was modeled so as to reduce computational overhead and encourage more rapid through-the-thickness failure. The uniaxial tensile loading in the model was applied as follows: in the tensile loading portion of the simulations (after the initial thermal cooldown load step) the total amount of displacement (from three subsequent loading steps) applied at the top edge of the specimen was 0.2 mm for a strain of 0.008 (over the specimen 25-mm gauge length). Table VIII provides the breakdown of the three sequential load steps of displacement showing the strain range of each load step, the number of displacement increments, and the displacement imposed per each increment for this specimen volume fraction.

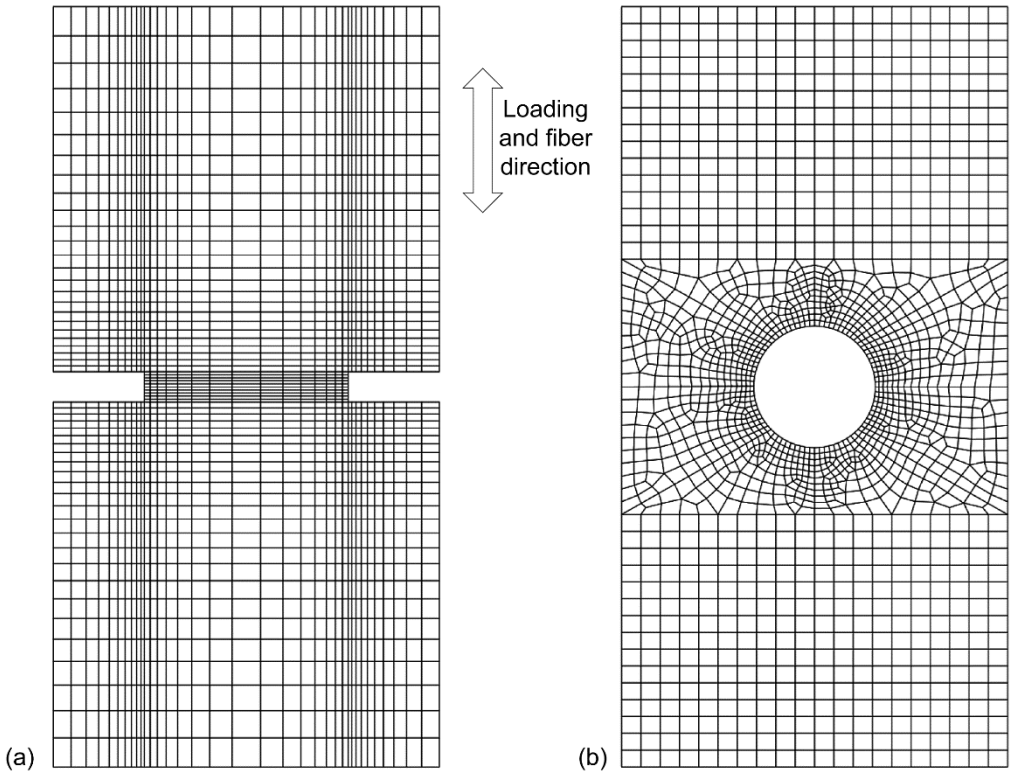

Figure 20.—Finite element meshes of specimens with 0°-oriented fibers. See Figure 4 for the local and global coordinate system reference frame for these specimens. (a) Double-notched specimen. (b) Central-hole specimen.

TABLE VIII.—LOAD STEP DESCRIPTION FOR SIMULATION OF DOUBLE-NOTCHED AND CENTRAL-HOLE SPECIMENS WITH LAMINATE CONFIGURATION OF 0°-ORIENTED 30-vol% FIBERS
[Total imposed displacement, 0.2 mm for 0.008 strain.]

Stress-strain curve region	Total displacement and strain	Strain range	Number of displacement increments	Displacement per increment, mm
First stage (load step 2)— Elastic response and initial matrix damage	0.01750 mm for 0.0007 strain	0.0 to 0.0007	100	0.000175
Second stage (load step 3)— Matrix cracking	0.07501 mm for 0.003 strain	0.0007 to 0.003	100	.0005750
Third stage (load step 4)— Mostly fiber controlled until ultimate failure	0.2 mm for 0.008 strain	0.003 to 0.008	100	.00125

Figure 21 shows the stress profile in the double-notched unidirectional tensile specimen just prior to a (matrix) damage initiation event for the σ_{11}, σ_{22}, and σ_{12} stress components. As expected, the highest stresses are along the notch tips—the most likely locations from which damage initiates. The high shear stresses along the notch corners are particularly noteworthy and likely play a role in the early damage progression in the matrix seen in the simulations that were performed for this specimen geometry.

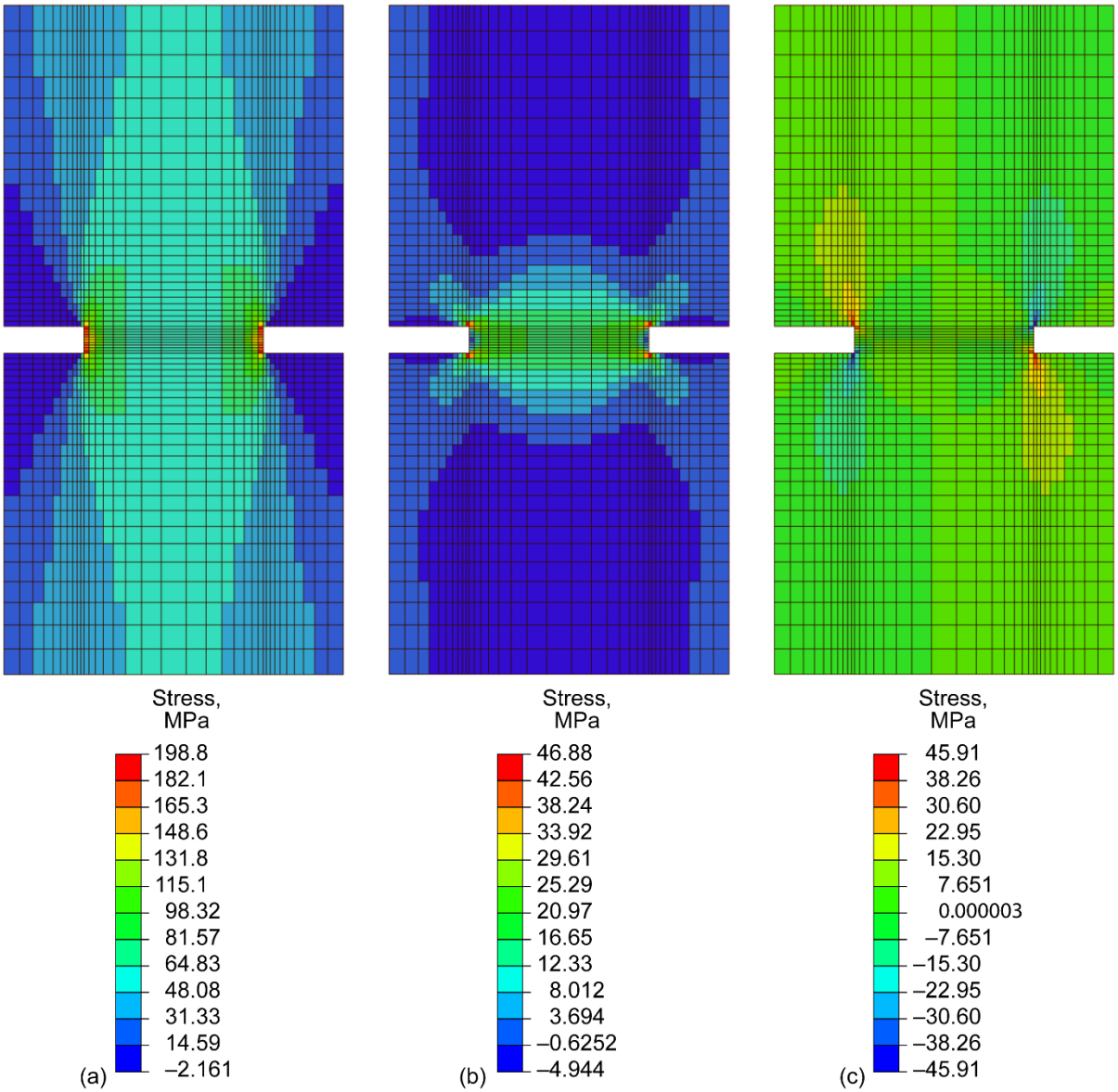

Figure 21.—Stress profile in the double-notched unidirectional tensile specimen just prior to a (matrix) damage initiation event. (a) σ_{11} stress profile. (b) σ_{22} stress profile. (c) σ_{12} stress profile.

Figure 22 shows the results from two simulations of the double-notched specimen plotting net-section-stress response against the imposed displacement imparted along the top edge of the specimen. Also shown for each simulation are the first matrix damage event, next when the matrix damage began propagating transverse to the loading direction, and finally the first fiber failure event. The two simulation curves closely follow the same track, which is similar to the trends observed in Figure 5. The deviation from one simulation to another only becomes apparent when the scale of the plot is magnified, similar to what was done in Figure 7 but not shown here. The tested matrix cracking stress from Bhatt and Phillips (1990) was 226±15 MPa. This seems to roughly correlate with the first matrix damage event, when the matrix damage began propagating transverse to the loading direction. The average ultimate tensile strength reported from Bhatt and Phillips (1990) was 650±135 MPa. In our two simulations, a path (across the specimen width) of elements with fiber failure occurred at 516 MPa. This was well below the experimentally measured value; however, it was not our aim here to accurately simulate ultimate strength. The experimentally measured values also had a significant scatter in reported values of ±135 MPa from the mean.

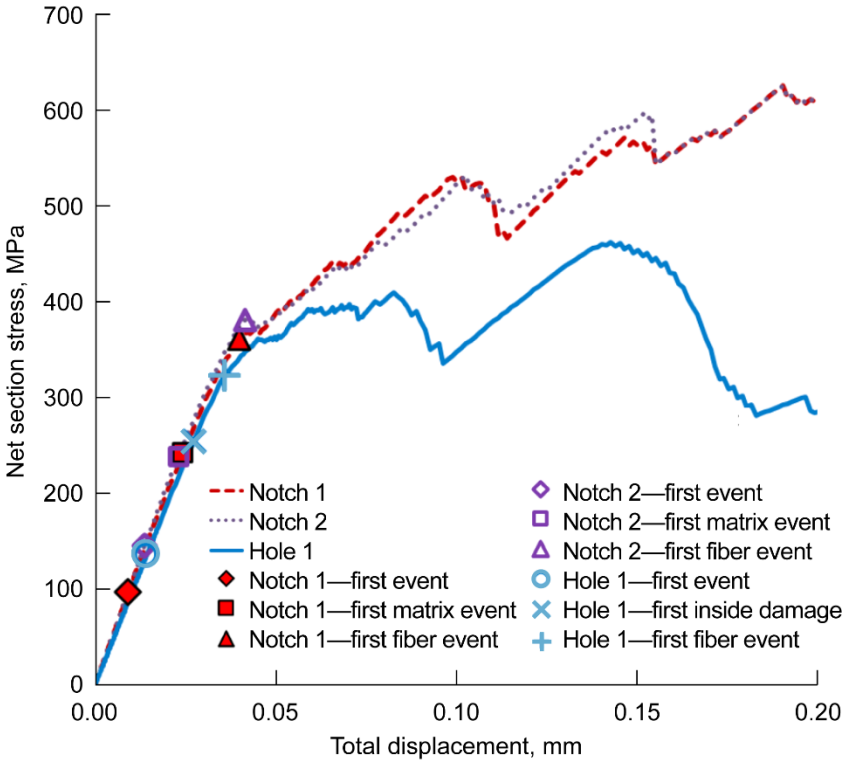

Figure 22.—Results from two simulations of the double-notched specimen and one simulation of a 0° unidirectional tensile specimen with a central hole, plotting net-section-stress response against the imposed total displacement along the top edge of the specimen imparted from the loading sequence. Also shown for each simulation are the first matrix damage event, next when matrix damage began propagating transverse to the loading direction, and finally the first fiber failure event.

Figure 23 shows the results from the two simulations showing the development of matrix damage up until the first fiber failure event for the double-notched specimen. Table IX provides the applied strains and net-section reaction stresses corresponding to Figure 23 from left to right. What can be seen in the figure is that axial splitting of the matrix between the fiber and matrix initiates first followed by matrix damage that develops transverse to the loading direction. The axial splitting is consistent with the failure mode that was observed by Bhatt and Phillips (1990) and reproduced here in Figure 19. Matrix damage in Figure 23 initiated along the notch face or corners and then propagated parallel to the direction of loading. At some point, the axial-splitting crack growth arrested and subsequent damage began to develop transverse to the direction of loading and within the region between where the axial splitting occurred.

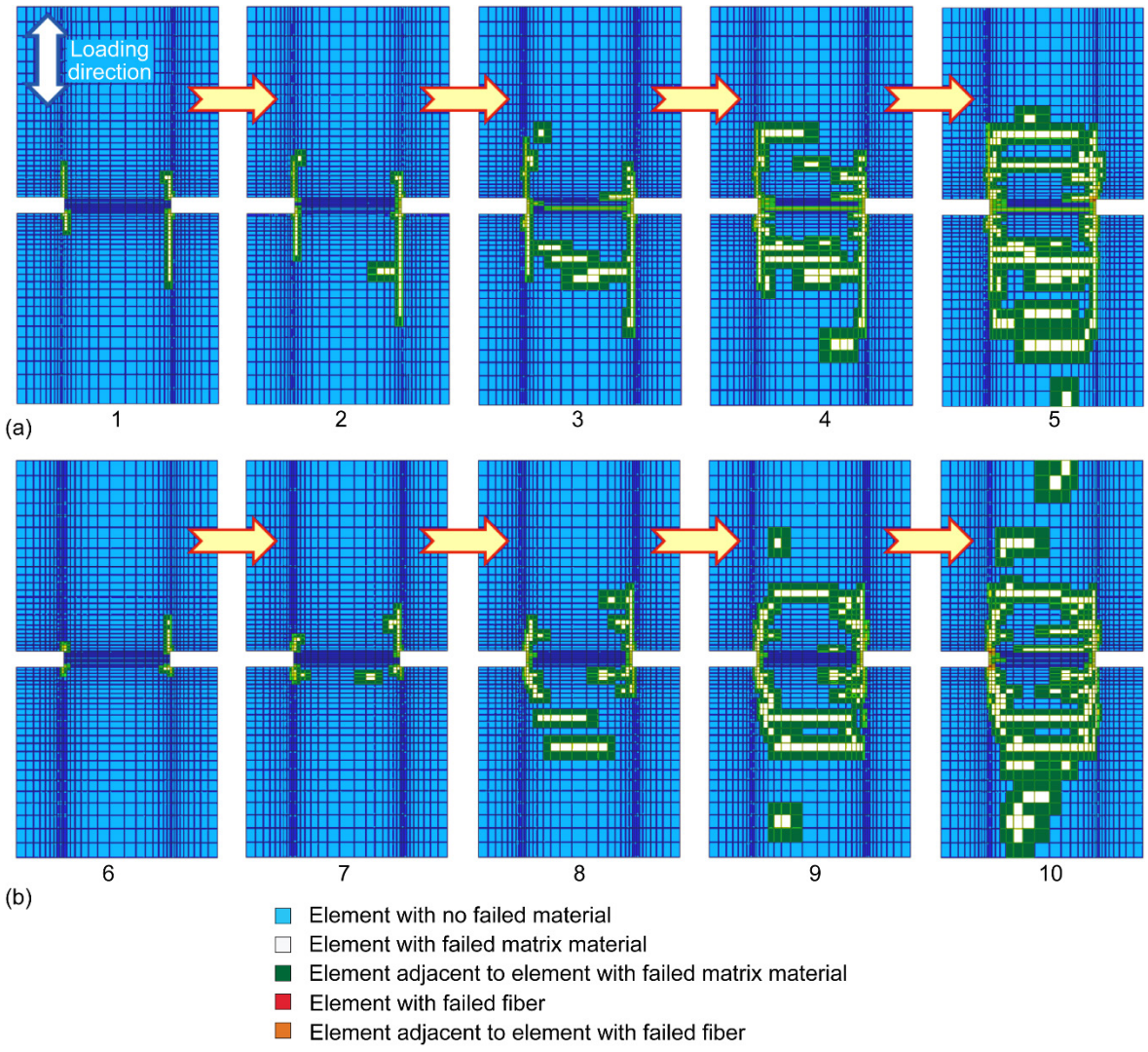

Figure 23.—Results from the two simulations of the double-notched specimen showing the development of matrix damage up until the first fiber failure event. (a) First simulation. (b) Second simulation.

TABLE IX.—APPLIED STRAIN AND NET-SECTION REACTION STRESS CORRESPONDING TO FIGURE 23 IMAGES

Applied strain (Net-section reaction stress, MPa)				
Image from Figure 23				
1	2	3	4	5
0.02038 (204.7)	0.02671 (263.1)	0.03188 (307.7)	0.03533 (333.1)	0.04501 (360.2)
6	7	8	9	10
0.02153 (222.7)	0.02671 (271.6)	0.03418 (333.6)	0.03878 (367.1)	0.04166 (380.4)

Therefore, the failure mode of axial splitting was correctly captured in the model. It could be argued that the refinement of the mesh in the regions of stress concentration and where axial splitting occurred influenced the development of the axial splitting damage pattern. This is true to a certain extent. We refined the mesh in this region to better capture this failure mode. However, if we had had a uniform refined mesh over the entire model of the gauge section, this failure mode would likely still have been reproduced. A coarse mesh would not have been able to reproduce this failure mode. So proper mesh refinement was a necessary ingredient to successful reproduction of the observed failure modes reported in Bhatt and Phillips (1990) in a computationally efficient manner.

We also simulated a 0° unidirectional tensile specimen with a central hole. This configuration was not tested by Bhatt and Phillips, but we included it so that the predicted failure modes for the two specimen configurations could be compared. Figure 24 shows the stress profile (σ_{11}, σ_{22} and σ_{12} stress components) of the central-hole unidirectional tensile specimen just prior to the (matrix) damage initiation event. The highest stresses, by a significant margin, are along the left and right edges of the hole for the σ_{11} stress component and are the most likely locations from which damage will initiate. The high σ_{11} stress along the hole edge are particularly noteworthy and probably play a key role in the early damage progression in the matrix seen in the simulations that were performed for this specimen geometry.

Referring back to Figure 22, results of one simulation of a 0° unidirectional tensile specimen with a central hole are compared with the two simulations of the double-notched specimen. The net-section-stress response is plotted against the imposed total displacement (imparted from the loading sequence) along the top edge of the specimen. Also shown are the first matrix damage event, next when matrix damage began propagating transverse to the loading direction, and finally the first fiber failure event. Even though only one simulation was performed for the central-hole specimen, the results for the first matrix damage event and the beginning of transverse matrix microcracking appear to be similar to those for the double-notch specimen. Deviation in the curves between the central-hole and notched specimens appears to occur at the net-section stress for the first fiber failure event. We expect that similar results would have been obtained had more simulations had been run; however, we believe that this was unnecessary because there were no experimental results with which to compare. We believe that the single simulation was sufficient to demonstrate the development of the overall failure modes for a central-hole specimen geometry.

Figure 25 shows the development of matrix damage until the first fiber failure event for the central-hole specimen, and Table X provides the applied strains and net-section reaction stresses corresponding to the Figure 25 images. The figure shows that matrix damage initiates along the outside edge of the hole where the highest stresses are and that it extends around a portion of the periphery of the hole before damage begins to extend radially from the center of the hole. Eventually transverse matrix cracking begins to develop prior to the first fiber failure damage event.

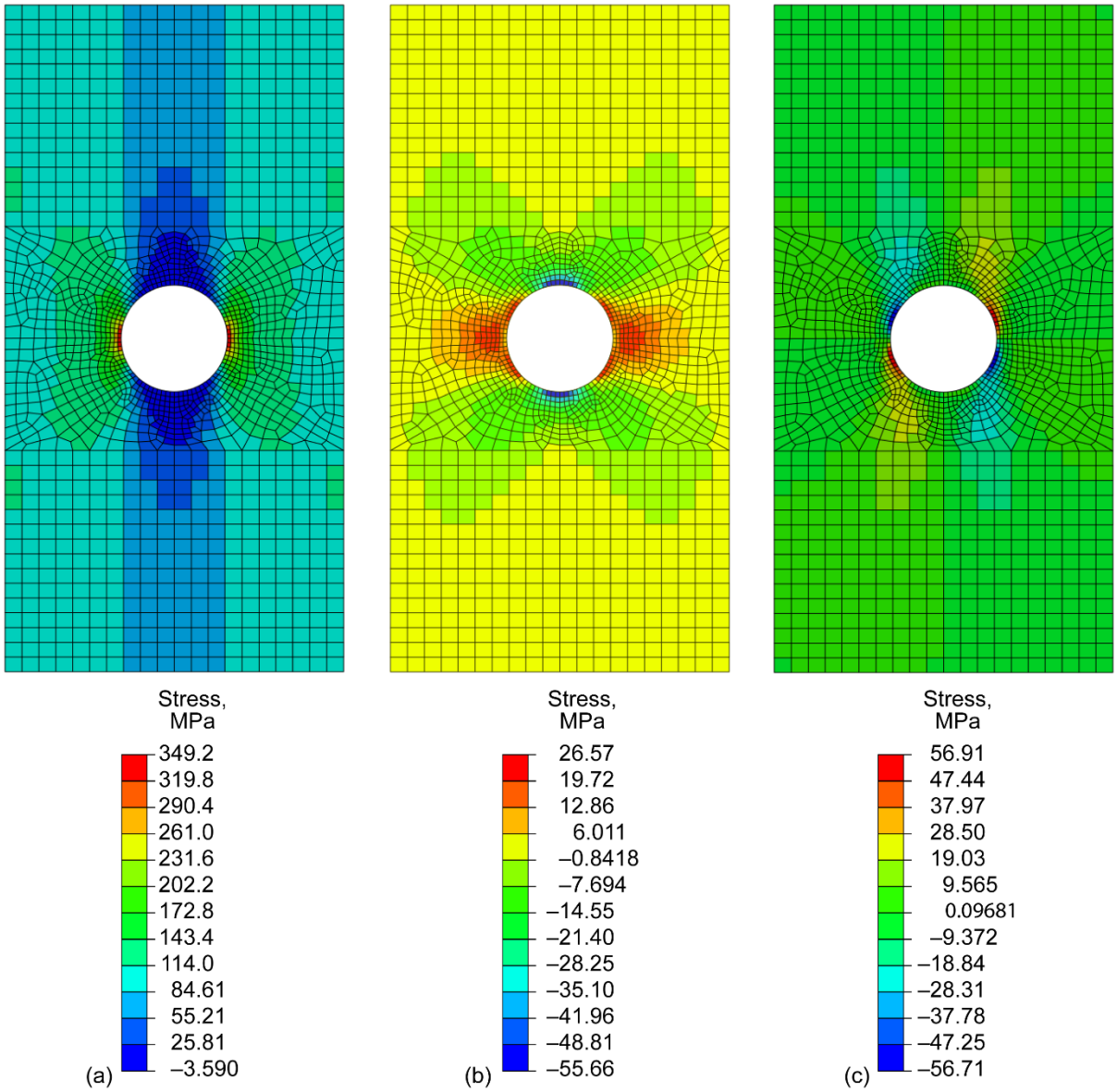

Figure 24.—Stress profile in the central-hole unidirectional tensile specimen just prior to a matrix damage initiation event. (a) σ_{11} stress profile, (b) σ_{22} stress profile, (a) σ_{12} stress profile.

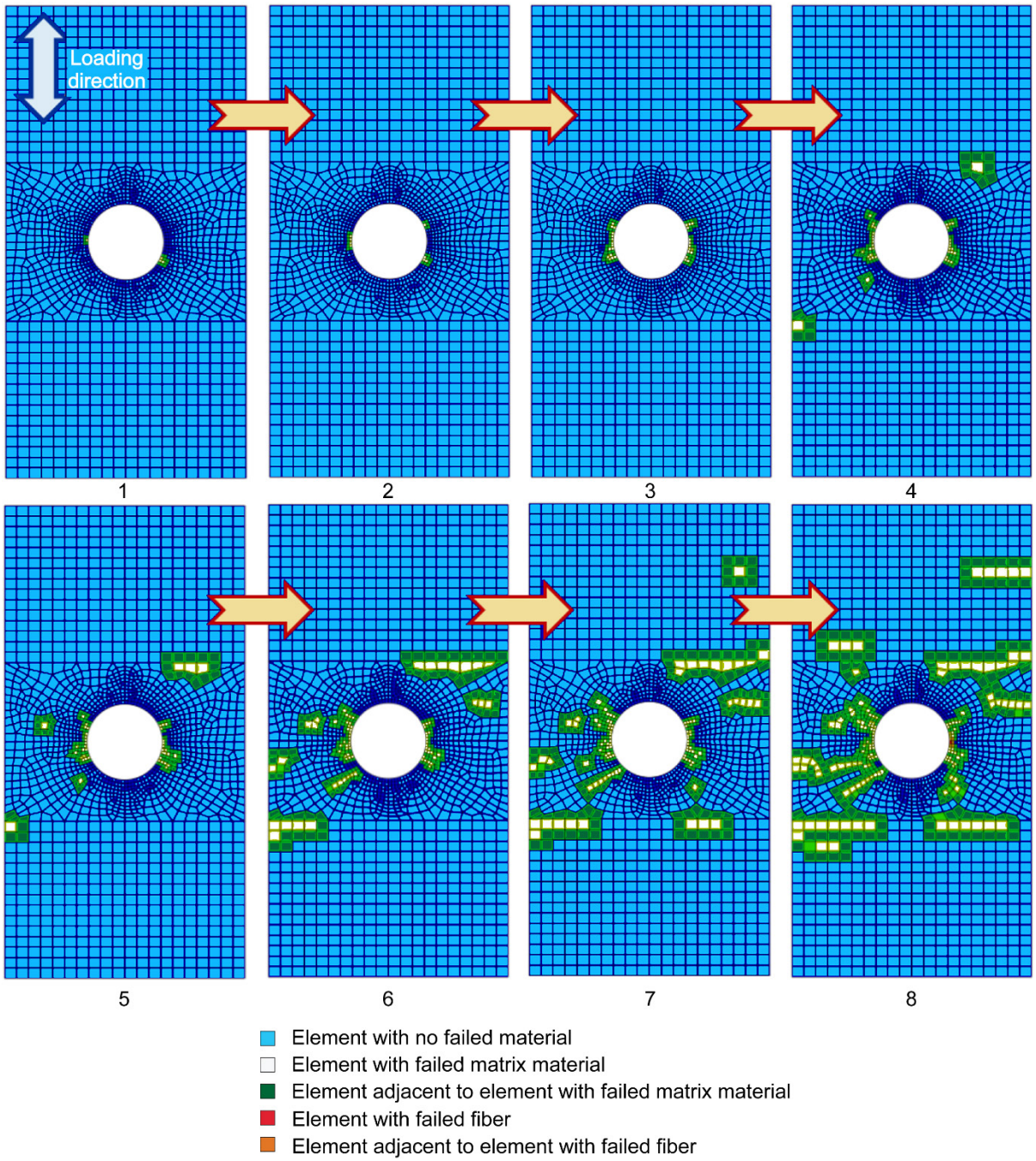

Figure 25.—Results from a simulation showing the development of matrix damage up until the first fiber failure event in the central-hole specimen.

TABLE X.—APPLIED STRAIN AND NET-SECTION REACTION STRESS CORRESPONDING TO FIGURE 25

Applied strain (Net-section reaction stress, MPa)			
Image from Figure 25			
1	2	3	4
0.01866 (176.0)	0.02153 (202.9)	0.02728 (254.7)	0.02843 (264.8)
5	6	7	8
0.02901 (269.9)	0.03188 (293.0)	0.03361 (306.9)	0.03591 (323.1)

5.0 Summary and Conclusions

The Finite Element Analysis—Micromechanics Analysis Code/Ceramics Analysis and Reliability Evaluation of Structures (FEAMAC/CARES) program was used to study the progressive damage response of silicon-carbide-fiber-reinforced reaction-bonded silicon nitride matrix (SiC/RBSN) composites under tension. The study analyzed $[0]_8$, $[10]_8$, $[45]_8$, $[90]_8$, $[0_2/90_2]_s$, and $[+45_2/-45_2]_s$ laminates, as well as doubled-edge-notched and central-hole $[0]_8$ laminates, which were studied to demonstrate the versatility and accuracy of the tool. Both quantitative and qualitative results correlated well with the available experimental data. The primary objective was to validate and benchmark the FEAMAC/CARES program. FEAMAC/CARES simulates stochastic-based discrete-event progressive damage of ceramic-matrix-composite and polymer-matrix-composite material structures. It couples three software programs: (1) the Micromechanics Analysis Code with Generalized Method of Cells (MAC/GMC), (2) the Ceramics Analysis and Reliability Evaluation of Structures Life Prediction Program (CARES/*Life*), and (3) the Abaqus finite element analysis program. For each FEAMAC/CARES simulation trial, the stochastic nature of brittle material strength results in random, discrete damage events, which incrementally progress until ultimate structural failure. The key findings or conclusions of this study follow:

(1) Progressive damage simulation of composite structures incorporating probabilistic material strength models is possible with the FEAMAC/CARES code.
(2) The unit sphere multiaxial model was successfully used to predict the strength response of a SiC/RBSN composite for various fiber orientations under uniaxial tension.
(3) Reasonable correlation to matrix cracking strength experimental data was achieved assuming that the matrix was an isotropic material with a Weibull modulus of $m \approx 5$ and that residual stresses from thermal processing were present.
(4) Brittle behavior versus nonbrittle failure (*graceful failure*) was demonstrated.
(5) The simulation methodology is capable of predicting scatter in proportional limit strength.
(6) Localized damage modes at stress concentration features are shown, and the axial-splitting failure mode for the double-notched tensile specimen was adequately reproduced.

References

Aboudi, J.; Arnold, S.M.; and Bednarcyk, B.A., 2013: Micromechanics of Composite Materials: A Generalized Multiscale Analysis Approach. Elsevier, Oxford, UK.

Bednarcyk, Brett A.; and Arnold, Steven M., 2002a: MAC/GMC 4.0 User's Manual—Keywords Manual. NASA/TM—2002-212077/VOL2. http://ntrs.nasa.gov

Bednarcyk, Brett A.; and Arnold, Steven M., 2002b: MAC/GMC 4.0 User's Manual—Example Problem Manual. NASA/TM—2002-212077/VOL3. http://ntrs.nasa.gov

Bednarcyk, Brett A.; and Arnold, Steven M., 2006: A Framework for Performing Multiscale Stochastic Progressive Failure Analysis of Composite Structures. Proceedings of the 2006 ABAQUS Users' Conference, Cambridge, MA.

Bhatt, Ramakrishna T., 1988: Effect of Fabrication Conditions on the Properties of SiC Fiber Reinforced Reaction Bonded Silicon Nitride Matrix Composites (SiC/RBSN). NASA TM–88814. Available from the NASA STI Program.

Bhatt, Ramakrishna T., 2014: Ohio Aerospace Institute, Cleveland, OH, private communication.

Bhatt, R.T.; and Phillips, R.E., 1990: Laminate Behavior for SiC Fiber-Reinforced Reaction-Bonded Silicon Nitride Matrix Composites. J. Compos. Tech. Res., vol. 12, no. 1, pp. 13–23.

Chulya, Abhisak; Gyekenyesi, John P.; and Bhatt, Ramakrishna T., 1991: Mechanical Behavior of Fiber Reinforced SiC/RBSN Ceramic Matrix Composites: Theory and Experiment. NASA TM–103688 (AVSCOM Technical Report 91–C–004). http://ntrs.nasa.gov

Dassault Systèmes Simulia Corp., 2011: Abaqus Analysis User's Manual, Version 6.11-1.

DiCarlo, J.A.; and Williams, W., 1980: Dynamic Modulus and Damping of Boron, Silicon Carbide, and Alumina Fibers. NASA TM–81422. http://ntrs.nasa.gov

Goldberg, Robert K., 2012: Utilization of the Generalized Method of Cells to Analyze the Deformation Response of Laminated Ceramic Matrix Composites. NASA/TM—2012-217737. http://ntrs.nasa.gov

Kalluri, Sreeramesh; Calomino Anthony M.; and Brewer, David N.: Computation of Variability in the Average Thermal and Mechanical Properties of a Melt-Infiltrated SiC/SiC Composite. High Temperature Ceramic Matrix Composites 5, M. Singh et al., eds., Proceedings of the 5th International Conference on High-Temperature Ceramic Matrix Composites (HTCMC 5), 2004, pp. 279–284.

Lamon, Jacques, 2001: A Micromechanics-Based Approach to the Mechanical Behavior of Brittle-Matrix Composites. Compos. Sci. Technol., vol. 61, pp. 2259–2272.

Liu, Kuang C.; and Arnold, Steven M., 2011: Impact of Material and Architecture Model Parameters on the Failure of Woven Ceramic Matrix Composites (CMCs) Via the Multiscale Generalized Method of Cells. NASA/TM—2011-217011. http://ntrs.nasa.gov

Murthy, Pappu L.N.; Chamis, Christos C.; and Mital, Subodh K., 1996: Computational Simulation of Continuous Fiber-Reinforced Ceramic Matrix Composites Behavior. NASA TP–3602. http://ntrs.nasa.gov

Murthy, Pappu L.N., et al., 2008: Probabilistic Analysis of a SiC/SiC Ceramic Matrix Composite Turbine Vane. Composites Part B, vol. 39, pp. 694–703.

Nemeth, Noel N.; Jadaan, Osama M.; and Gyekenyesi, John P., 2005: Lifetime Reliability Prediction of Ceramic Structures Under Transient Thermomechanical Loads. NASA/TP—2005-212505. http://ntrs.nasa.gov

Nemeth, Noel N., 2014: Unit-Sphere Multiaxial Stochastic-Strength Model Applied to a Composite Material. J. Compos. Mater., vol. 48, no. 27, pp. 3395–3424.

Nemeth, Noel N., et al., 2016: Stochastic-Strength-Based Damage Simulation Tool for Ceramic Matrix and Polymer Matrix Composite Structures. NASA/TM—2016-219113.

Saigal, A., et al., 1993: Thermal Residual Strains and Stresses in Silicon Carbide-Fiber-Reinforced Silicon Nitride Composites. Compos. Eng., vol. 3, no. 11, pp. 1075–1086.